N91-22987

OBLIQUITY HISTORIES OF EARTH AND MARS: INFLUENCE OF INERTIAL AND DISSIPATIVE CORE-MANTLE COUPLING; Bruce G. Bills, LPI, Houston, TX

For both the Earth and Mars, secular variations in the angular separation of the spin axis from the orbit normal are suspected of driving major climatic changes (1,2,3,4). There is thus considerable interest in determining, as accurately as possible, the amplitude and timing of these obliquity variations. If the orientation of the orbital plane were inertially fixed, and the planet were to act as a rigid body in its response to precessional torques, the spin axis would simply precess around the orbit normal at a fixed obliquity ϵ and at a uniform angular rate $\alpha \cos(\epsilon)$. The precession rate parameter

$$\alpha = \frac{3}{2} \frac{(C-(A+B)/2)}{C\omega} \sum \mu_i/(b_i)^3 \qquad [1]$$

depends on the principal moments of inertia ($A \leq B \leq C$) and rotation rate ω of the perturbed body, and on the gravitational masses $\mu = GM$ and semiminor axes $b = a(1-e^2)^{1/2}$ of the perturbing bodies. For Mars, the precession rate is not well known, but probably lies in the interval 8-10 arcsec/year (5,6,7,8,9,10). The much larger precession rate for the Earth (~50.3 arcsec/year) is partly due to greater proximity to the Sun (which contributes roughly 1/3 of the total), but is mostly due to the presence of the Moon (11).

Gravitational interactions between the planets lead to secular motions of the orbit planes of the form

$$\sin(I)\, e^{i\Omega} = \sum N_j e^{i(s_j t + \delta_j)} \qquad [2]$$

where I and Ω are the inclination and longitude of the node, and N_j, s_j and δ_j are amplitudes, rates and phase constants (12,13). In the rigid body case, the spin axis still attempts to precess about the instantaneous orbit normal, but now the obliquity varies. A first order solution for the obliquity can be written in a form similar to [2] but with amplitudes $K_j N_j$, where the admittance K_j has the value (14,15,16)

$$K_j = \frac{s_j}{s_j + \alpha \cos(\epsilon)} \qquad [3]$$

As the orbital precession rate constants s_j are all negative and fall within the range {-26.3 arcsec/year $\leq s_j \leq 0$}, while the spin precession rate constants are positive, the potential exists for significant resonant amplification of the obliquity if the denominator of [3] approaches zero (17,18). The possibility of actual singularities in [3] is not too worrisome, as the linear analysis leading to that form of the admittance is no longer applicable in the immediate vicinity of a resonance. However, the physical model of rigid rotation which leads to that formula is almost certainly too simplistic.

The hydrostatic figure of a planet represents a compromise between gravitation, which attempts to attain spherical symmetry, and rotation, which prefers cylindrical symmetry (19). Due to their higher mean densities, the cores of the Earth and Mars will be more nearly spherical than the outer layers of these planets. The direct gravitational torques on the core will thus be inadequate to make it precess at the same rate as the mantle. For the Earth, where the structure is relatively well known, the core oblateness is only about 3/4 that required for coprecession with the mantle (20). However, it is clearly the case that the core and mantle precess at very nearly the same rate (21,22). Two different types of torques contribute to the coupling.

CORE-MANTLE COUPLING: Bills, B.G.

On short time scales it is appropriate to consider the core to be an invisid fluid constrained to move within the ellipsoidal region bounded by the rigid mantle (23,24). The inertial coupling provided by this mechanism is effective whenever the ellipticity of the container exceeds the ratio of precessional to rotational rates. If the mantle were actually rigid, or even elastic, this would be an extremely effective type of coupling. However, on sufficiently long time scales, the mantle will deform viscously and can accomodate the motions of the core fluid. The inertial coupling torque exerted by the core on the mantle will have the form $T_i = k_i [\omega_m \times \omega_c]$. A fundamentally different type of coupling is provided by electromagnetic or viscous torques (25,26). The dissipative coupling torque exerted by the core on the mantle will have the form $T_d = -k_d [\omega_m - \omega_c]$. This type of coupling is likely to be most important on longer time scales. In each case, the mantle exerts an equal and opposite torque on the core.

The admittance which relates inclination amplitude to obliquity amplitude is now a complex quantity which can be written in the following form (27,28)

$$K(s) = \frac{s(s + a_m + \eta)}{(s + a_m)(s + a_m + \eta) - \Delta a\, \eta_m} \qquad [4]$$

The coupling constants are rescaled ($\beta_m = k_d/C_m$, $\gamma_m = \omega \cos(\epsilon)\, k_i/C_m$) and then combined to form a single complex parameter $\eta_m = \gamma_m - i\beta_m$. Also, $a_m = \alpha_m \cos(\epsilon) + \cos(I)\, d\Omega/dt$. Core parameters ($a_c, \beta_c, \gamma_c, \eta_c$) are defined analogously, and the sum of core and mantle parameters $\eta = \eta_m + \eta_c$ is left unsubscripted, and $\Delta a = a_m - a_c$. Viscous relaxation of the mantle is included by multiplying both γ values by $(is\tau)/(1+is\tau)$, where τ is the effective Maxwell relaxation time of the mantle.

There are several features to note, in comparing [3] and [4]. As is typical of a forced oscillation with damping, the response now lags the forcing by an amount which depends on the frequency of forcing and the strength of the viscous coupling. The most evident difference in response is near resonance, since [4] exhibits no singularities. However, even away from resonance, the inclusion of possible differential precession can modify the obliquity history by amounts that could have climatic significance. Unfortunately, the coupling constants are not well known, even for the Earth, and are almost completely unconstrained for Mars. Thus, some caution is advised in constructing climatic history scenarios which depend on details of the obliquity history.

References: (1) M. Milankovitch, Konin. Serbische Akad., 484p, 1941; (2) A.L. Berger et al. (eds.) Milankovitch and Climate, D. Reidel, 1984; (3) O.B. Toon et al., Icarus 44, 552-607, 1982; (4) S.M. Clifford et al., Eos 47, 1585-1596, 1988; (5) P. Lowell, Astron. J. 28, 169-171, 1914; (6) W.M. Kaula, Geophys. Res. Lett. 6, 194-196, 1979; (7) B.G. Bills, Geophys. Res. Lett. 16, 385-388, 1989; (8) B.G. Bills, Geophys. Res. Lett. 16, 1137-1338, 1989; (9) A.T. Sinclair, Astron. Astrophys. 220, 321-328, 1989; (10) T.A. Morley, Astron. Astrophys. (in press) (11) H. Kinoshita, Celest. Mech. 15, 277-326, 1977; (12) P. Bretagnon, Astron. Astrophys. 30, 141-154, 1974; (13) J. Laskar, Astron. Astrophys. 198, 341-362, 1988; (14) S.G. Sharaf, & N.A. Budnikova, Trud. Inst. Teor. Astron. 11, 231-261, 1967. (15) W.R. Ward, J. Geophys. Res. 1974; (16) A. Berger, Celest. Mech. 15, 53-74, 1977; (17) W.R. Ward et al., J. Geophys. Res. 83, 243-259, 1979; (18) W.R. Ward, Icarus 50, 444-448, 1982; (19) Z. Kopal, Figures of Equilibrium of Celestial Bodies, U. Wisc. Press, 1960; (20) M.L. Smith & F.A. Dahlen, Geophys. J. R. Astr. Soc. 64, 223-281, 1981; (21) E.C. Bullard, Proc. Roy. Soc. A197, 433-453, 1949; (22) F.D. Stacey, Geophys. J. R. Astr. Soc. 35, 47-55, 1973; (23) H. Poincare, Bull. Astr. 27, 321-356, 1910; (24) A. Toomre, Geophys. J. R. Astr. Soc. 38, 335-348, 1974; (25) S. Aoki, Astron. J. 74, 284-291, 1969; (26) M.G. Rochester, J. Geophys. Res. 67, 4833-4836, 1962. (27) P. Goldreich & S.J. Peale, Astron. J. 75, 273-284, 1970; (28) W.R. Ward & W.M. DeCampli, Astrophys. J. Lett. 230, 117-121, 1979.

Implications of the low carbonate abundance in the optical surface of Mars. **Diana L. Blaney. Planetary Geosciences Division, Hawaii Institute of Geophysics, 2525 Correa Rd. Honolulu, HI 96822.**

There are two major reasons for expecting carbonates on Mars: 1) if Mars underwent a period of climatic warming due to a thicker CO2 atmosphere, carbonates would have formed at a rapid rate (1,2) and 2) the thermodynamically stable weathering products of igneous material on Mars under current conditions also include carbonates (3). Earth-based spectroscopy of the Martian surface in the 4.0 μm region has placed an upper limit on the carbonate abundance of < 1 - 3 wt% in the optical surface of the regions measured based on laboratory mixing models (4,5). The implications for weathering and climate change on Mars using various models to explain the low carbonate abundance are presented.

Model 1. The observed upper limit on carbonate abundance (i.e. <1 wt%) is representative of the Martian regolith. A 1 km mega-regolith with 1 wt% carbonate could at most contain 0.6 bars of CO2 (2), well short of the 3-5 bars (2,6,7) needed for global warming by a CO2 greenhouse at average orbital parameters.

A consequence of an early wet warm Mars is that liquid water would be present to remove CO2 from the atmosphere by formation of carbonates would occur at rates of approximately 1 bar CO2 removed every 10^7 years (1,2). If the low carbonate abundance observed (0.6 bars), accurately reflects the planetwide inventory, then a 3-5 bar early greenhouse lost most of its CO2 by other mechanisms and had a duration of a few million years. A short greenhouse contradicts the geomorphic evidence which shows valley networks (a major geomorphic feature supporting an early greenhouse), forming during throughout the first billion years. Recycling carbonate to replenish the atmospheric CO2, whether by volcanic (2) or by impact (8) processes, may be able to extend the length of the greenhouse, but the last few bars would have to have been stored in the near surface environment (i.e. if you are forming carbonates by surface water, the last carbonates formed must be near the surface).

A low carbonate abundance would also imply that the weathering products observed (i.e. the dust) are not the thermodynamically stable end-members of weathering under current ambient Martian conditions. As an illustration, consider the thermodynamically stable decomposition products from the weathering of basalt of the same composition as Shergotty. Shergotty is a basaltic achondrite from the SNC (S=Shergotty, N=Nakhla, and C=Chassigny) group of meteorites. SNC are thought for a variety of reasons to come from Mars (e.g. 9). The weathering products of a Shergotty-like basalt which has reached thermodynamic equilibrium by gas-solid interactions at 240°K and current Mars atmospheric conditions, based on (3) indicate a total carbonate abundance of 32.48 wt %. If the 1 wt% carbonate in the dust is a reasonable upper limit, then about only about 3% of the dust could have formed by gas solid reactions carried to equilibrium. The majority of the dust would have formed by other processes. Similarly, if liquid water containing dissolved CO2 and O2 from the current Mars atmosphere were involved, again based on (3), the end products would contain 18.07 wt% carbonate, leaving 5.5 wt% of the dust to form by this process. Clearly, either the majority of the dust formed by processes other than surface weathering under current ambient conditions, or the formation process has been halted mid-way by kinetic barriers leaving metastable products.

Model 2. Carbonate deposits are located at depth. Carbonates deposits at depth are impossible to detect with spectroscopy, as spectroscopy looks only at the optical surface. Previous models calling for the recycling of carbonates to sustain an early greenhouse (2,8) assume that carbonates are well mixed in the regolith. Carbonate recycling rates from both impact and volcanic burial are too slow to replenish the carbon dioxide fixed as carbonates by liquid water (8). Carr (1989) suggested that the rate of carbonate fixation may have been overestimated. If liquid water was not continuously present on the surface, then carbonate formation would have preceded at a much slower rate. Temperatures, while warmer than the current epoch, would have remained just below the point at which liquid water could exist. Ground water would be close to the surface and under proper hydrostatic conditions would break out and form valley networks. Even with the slower carbon dioxide fixation rates, carbonates would form in the near surface environment where they should be detectable. Thus, a mechanism to for locating carbonates at depth is needed.

An alternative hypothesis calls for stratified carbonate layers. If carbonates exist at depth in stratigraphically localized deposits a possible formation scenario could be: a) Mars is warm, valley networks form; b) carbonates form rapidly, decreasing the atmospheric CO2 pressure until temperatures drop below the temperature needed to keep liquid water around to form carbonates; c) carbonate formation ceases and volcanic and impact processes bury the carbonates; d) carbonates are buried to a depth where rapid decrepitation occurs, releasing a pulse of CO2; e) the released CO2 causes another episode of greenhouse warming and valley network formation, and carbonates begin to form again. If a carbonate decrepitation depth of about 17 km, as suggested by Carr (1989), is valid then the cycle of rapid carbonate formation followed by burial could repeat itself about 10 times in the first billion years according to liquid stirring models (8). Declining impact rates would then slow the burial rates, leaving the carbonate layer stratified somewhere in the Martian crust. There is some geomorphic evidence for a strength discontinuity at about 1 km depth (10) which

could be a carbonate layer. Geochemical arguments which focus on the calcium deficiency of the Viking fines when compared to SNC meteorites also indicate that a carbonate layer may be present at depth (11).

Model 3. The low carbonate abundance is the result of secondary weathering processes which have removed carbonates from the regolith. The presence of the sulfate in the Martian fines measured by Viking Landers 1 and 2 (12), may have major implications for carbonate abundance.

The stability of carbonates in the presence of gaseous SO2 has been addressed by (13) and (14) with differing results. Clark et. al. (13) performed laboratory experiments which indicated that carbonates decompose readily in the presence of SO2 leaving sulfates. Sidorov and Zoltov (14) examined kinetic constraints and showed that the reaction encounters a kinetic barrier which would make this reaction negligible. Understanding the possible role of SO2 in destroying carbonates is critical in understanding the composition and evolution of the fines at the Martian surface. Alteration of the surface by airborne reactive components may be a major process in the formation of salts on Mars.

Settle (15) proposed a sulfate aerosol model for the formation of the sulfate duracrust at the Viking sites. The acidic nature of these aerosols would tend to decompose carbonates readily. If carbonates do decompose in the presence of SO2 vapor or sulfate aerosols, CO2 would be released from the decomposed carbonates back into the Martian atmosphere. A terrestrial example of aerosol formed salts are the sulfate and nitrate deposits form in Antarctica from the deposition of stratospheric anions, which react with local rocks which provide the cations to form these deposits (16).

Carbonates and sulfates must be considered together. If carbonates are absent from the surface due to interactions with volcanic aerosols, then the rate of SO2 released by volcanoes on Mars must be greater than the rate of regolith overturn exposing new carbonates. Fresh craters which have occurred after the height of volcanism would be expected to show evidence of carbonates brought up from depth. The rates of both volcanism and cratering were higher during the early portion of Martian history than at the present (e.g. 17, 18). If the sulfur in the Martian regolith is the result of sulfate aerosol deposition throughout Martian history, then the release of CO2 by sulfate aerosols may have played a critical role in the rapid recycling of CO2 throughout Martian history.

Model 4. Weathering environments on Mars did not form carbonates. The majority of materials examined on the Martian surface are weathering products formed by unknown mechanisms. As discussed previously, the expected carbonates from surface atmospheric interactions do not seem to be present in large quantities in the optical surface of Mars. Processes unique to Mars may have formed the observed dust. A weathering mechanisms which may have created the dust is impact ejecta from volatile rich targets (19).

In addition to the hydrothermal alteration of material in throughout sheets, Kieffer and Simonds (19) proposed that a fine ash deposit formed by the rapid expansion of silicate melt/vapor by superheated steam from pore water or by carbon dioxide from decrepitated carbonates. The ash formed by the interaction of melt and vapor and would occur at the top of the crater's stratigraphic sequence. Erosion has removed this ash layer from terrestrial craters which, by analogy with melt sheets from impacts into crystalline material, would be 1-5% of the volume excavated. Impacts into volatile rich material provide a way of producing a large volume of fine grained material of unknown composition. The alteration of the melt in the vapor cloud would be controlled by the dominant volatile propelling the expansion of the melt-vapor cloud. Thus, if water was the principle volatile, oxidation and hydration products would dominate and little if any carbonate would form. Due to the speed with which this event would occur, the altered material would be poorly crystalline or crystalline on a small scale.

References: 1. Fanale F. P. et al., *Icarus, 50,* 381-407, 1982. 2. Pollack, J. B. et al., *Icarus ,71,* 203-224, 1987. 3. Gooding, J.L., *Icarus, 33,* 483-513, 1978. 4. Blaney, D.L., and T.B. McCord,*J. Geophys. Res., 94,* 10,159-10,166,1989. 5. Blaney, D.L. and T.B. McCord, submitted to *J. Geophys. Res.,* 1990. 6. Pollack, J. B, *Icarus* **37,** 479-553, 1979. 7. Postowko S.E. and W.R. Kuhn, *J. Geophys. Res., 82,* 4635-4639, 1986. 8. Carr, M. H., *Icarus,* in press, 1989. 9. McSween, H.Y.,*Rev. Geophys., 23,* 391-416, 1985. 10. Soderblom L.A. and D.B. Wenner, *Icarus,* 34, 622-637, 1978. 11. Warren, P.H., *Icarus, 70,* 153-161, 1987. 12. Clark, B.C. et al., *J. Geophys. Res.,87,* 10,059-10,068, 1982. 13 Clark B.C.e al. *J. Mol. Evol.,* 14, 91-102, 1979. 14. Sidorov Yu. I. and M. Yu Zolotov, In S.K. Saxena (ed.), *Chemistry and Physics of Terrestrial Planets,* Adv. Geochem. Vol. 6, Springer-Verlag, New York, p. 191-223, 1986. 15. Settle, M., *J. Geophys. Res., 84,* 8,343-8,354, 1979. 16. Campbell, I.B., and G.G.C. Claridge, *Antarctica: Soils, Weathering Processes and Environment, Developments in soil science 16,* Elsevier Science Pub. B.V., New York, N.Y., 1987. 17. Greeley, R. and P. Spudis, *Rev. of Geophys. and Space Phys., 19* , 13-41, 1981. 18. Neukum, G. amd K. Hiller, *J. Geophys. Res, 86,* 3097-3121, 1982. 19. Kieffer, S.W., and C.H. Simonds, *Rev.of Geophys. and Space Phys., 18,* 143-181, 1980.

Earth-Based Telescopic Observations of Mars in the 4.4 μm to 5.1 μm Region. **Diana L. Blaney and Thomas B. McCord. Planetary Geosciences Division, Hawaii Institute of Geophysics, 2525 Correa Rd. Honolulu, HI 96822.**

Measurements. The telescopic measurements of Mars reported here were made on August 19, 1988 UT at the NASA IRTF facility. Spectra were obtained with the Cooled Grating Array Spectrometer (CGAS) which utilizes a thirty-two element InSb line array with a resolution of R=300. Measurements were made by taking data at two different grating positions, with an eleven channel overlap between positions. Segment 1 covered 4.405 μm - 4.86 μm, and segment 2 covered 4.67 μm - 5.13 μm. Spectra were normalized to unity at 4.71 μm and were reduced using the star BS437 as a standard. A 2.7 arc-second aperture was used, producing a spot size 900 km in diameter at the sub-earth point. The measurements were taken as part of a sequence of measurements which also covered the wavelength region between 3.2 μm and 4.2 μm using three grating positions discussed(1).

The Martian atmosphere has a large number of atmospheric absorptions from both CO and CO2 in the wavelength region between 4.4 μm and 5.1 μm in addition to significant thermal components. These complications must be considered in the interpretation of the spectra.

Detection of an Absorption Feature at ~4.5 μm--Indication of Sulfates. A modeled atmospheric spectra (PCO2 =7 mbar, T=240K, CO/CO2=0.002, Airmass = 2.0) based on atmospheric models by Encrenaz is plotted over the spectra from the Argyre region (Figure 1). Note that all the atmospheric absorption features (shown with arrows) are clearly present in the telescopic data and that most features appear to be weaker than predicted by the model. The exception to this is the rise out of the 4.2 μm - 4.4 μm CO2 absorption which has a much shallower slope in the telescopic data than in the model atmosphere spectra. In addition to this gradual slope, an inflection at 4.5 μm is present in all the spectra and is extremely well defined in the Eastern Solis Planum and Argyre spectra (Figure 2). These measurements indicate that a surface absorption, centered near 4.5 μm, is present on the Martian surface.

The wavelength region between 4.4 μm and 5.1 μm contains sulfate absorptions, shown in figure 3a, for anhydrite, gypsum, and MgSO4, with the the 2ν3 vibrational overtone of the SO4-2 anion being centered at 4.5 μm.

The multiband structure seen in the sulfate spectra is produced by the metal cation complexing with the SO4 -2 lowering the symmetry of the sulfate. The lower symmetry causes degeneracy in the ν3 and ν4 modes, and the appearance of the ν1 and ν2 modes which are not infrared active under the tetrahedral symmetry that the SO4 -2 anion occupies. Unfortunately the Mars atmosphere cuts off the short wavelength portion of the absorption. The sulfates shown in figure 3a are shown in figure 3b at the resolution and wavelength of the telescopic data. Note that there does not appear to be any of the structure associated with the sulfates shown above in figures 3 a and b present in the telescopic data.

The location of this feature at 4.5 μm, the 2ν3 SO4 overtone, is especially exciting as the Viking lander sites detected large quantities of sulfur (~7 wt% SO3) in the Martian soils. The sulfur content was highly variable even at a local level. Sulfur abundance ranged from 5.9 wt% to 9 wt% SO3 at Chryse and from 7.6 wt% to 8.5 wt% SO3 at Utopia (2).

Spatial Variation in the 4.5 μm band depth -- Implications for sulfate distribution. In order to isolate atmospheric effects from surface absorptions we compared spectra which had the same 3.81 μm band depth. The 3.81 μm band is caused by CO2 with 16O and 17O (1). The isotopically heavy CO2 absorption provides an indicator, independent of possible sulfate absorption, of the similarity of atmospheric conditions of the various spectra. The spectra for the regions Valles Marineris, Argyre Basin, Eastern Solis Planum and Eastern Tharsis (figure 2) all have 3.81 μm band depth between 3.1% and 3.3%.

In comparing the Valles Marineris, Argyre Basin, Eastern Solis Planum and Eastern Tharsis spectra, the 4.5 μm inflection discussed above is probably the strongest indicator of sulfate abundance. In order of strength of deepest absorption to weakest the regions are ordered 1. Eastern Solis Planum, 2. Argyre Basin, 3. Eastern Tharsis, and 4. Valles Marineris, although in no spectrum does the rise out of the carbon dioxide band match the atmospheric model. A note of caution must be offered in taking this approach to estimating relative sulfate abundance as the strength of the 4.5 μm band could indicate not only the abundance but changes in mineralogy and degree of crystallization. However, the four regions do follow a progression due to either sulfate abundance or chemistry and there is significant variation between regions shown in figure 2.

Conclusions. The rise out of the 4.2 μm - 4.4 μm CO2 band cannot be matched by solely atmospheric constituents. A surface absorption must be added at roughly 4.5 μm in order to decrease the reflectance rise and produce the 4.5 μm inflection which is present in the data. The known presence of sulfates on the Martian surface and the location of this feature at the 2ν3 overtone of the SO4 -2 anion indicate that the surface absorption is probably caused by sulfates on the Martian surface. An exact match to a terrestrial sulfate mineral has not been made but it is suggested that the mineral has very weak structure and thus a high degree of symmetry . Significant variation exists between the spectra at 4.5 μm. In order of strength of deepest absorption to weakest the regions are ordered Eastern Solis Planum, Argyre Basin, Eastern Tharsis, and Valles Marineris for the four regions measured at similar Mars atmospheric conditions.

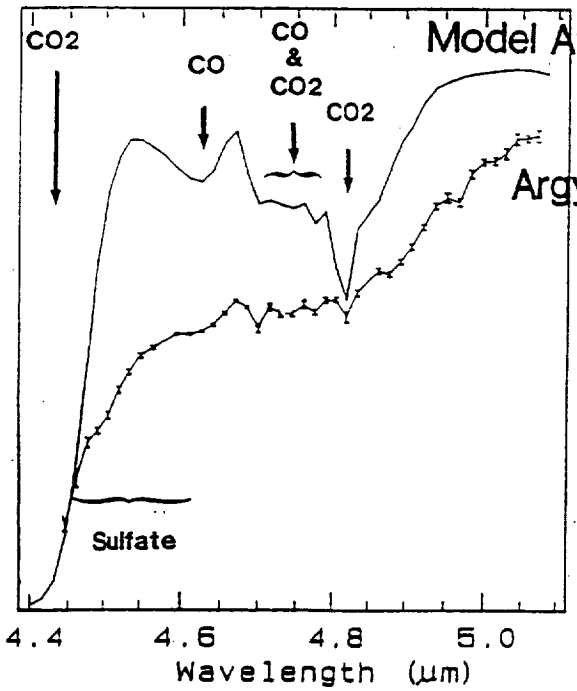

Figure 1. Representative spectra (Argyre region) and Mars model atmosphere of 7 mbar, 2 airmass, 240K, and CO / CO2 with atmospheric and surface absorptions labeled.

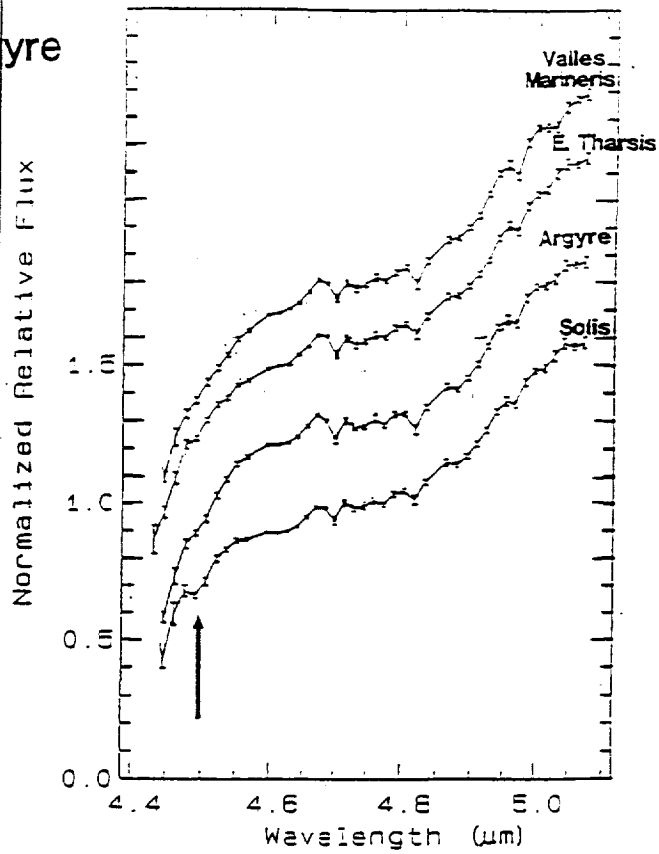

Figure 2. Spectra for four regions with similar 3.81 μm band depths. Regions are Eastern Solis Planum, Ridged Plains, Heavily Cratered Terrain; Argyre Basin; Eastern Tharsis; and Valles Marineris. Spectra are arranged in order of 4.5 μm band depth.

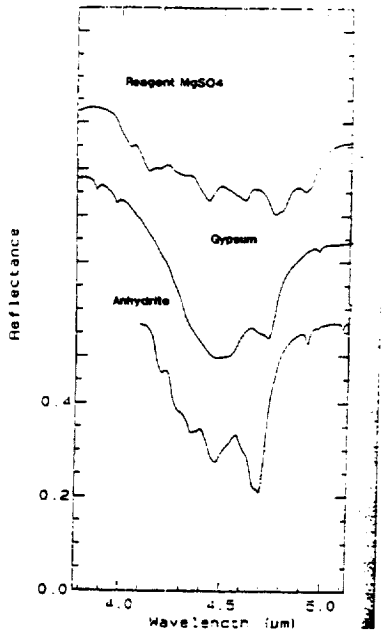

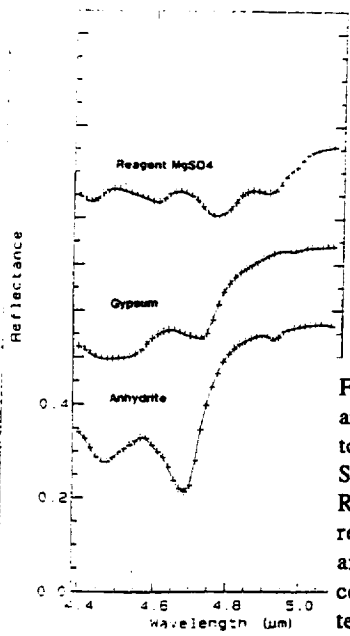

Figure 3 a. Reagent MgSO4, gypsum, and anhydrite reflectance spectra. Spectra are relative to sulfur and have a grain size of <34 μm. Spectra measured at 2 cm $^{-1}$ resolution. b. Reagent MgSO4, gypsum, and anhydrite reflectance spectra. Spectra are relative to sulfur and have a grain size of <34 μm. Spectra convolved and interpolated to wavelengths of the telescopic observations.

References: 1. Blaney D.L. and T.B. McCord submitted to *J. Geophys. Res.* 1990. 2. Clark, B.C. et al. *J. G. Res.* 87, 10,059-10,068, 1982.

RADIATION DAMAGE IN GERMANIUM DETECTORS: IMPLICATIONS FOR THE GAMMA-RAY SPECTROMETER OF THE MARS OBSERVER SPACECRAFT; J. Brückner, M. Körfer, and H. Wänke, Max-Planck-Institut für Chemie, Mainz, F. R. Germany; A. N. F. Schroeder, Universität zu Köln; F. R. Germany; D. Filges and P. Dragovitsch, Institut für Kernphysik, KFA Jülich, F. R. Germany; P. A. J. Englert, San Jose State University, CA, USA; R. Starr and J. I. Trombka, NASA Goddard Space Flight Center, MD, USA; I. Taylor, Princeton Gamma-Tech, NJ, USA; D. Drake and E. Shunk, Los Alamos National Laboratory, NM, USA.

High-purity germanium (HpGe) detectors will be used in space missions to measure gamma-rays emitted by planetary bodies or astronomical sources. The upcoming NASA Mars Observer mission, scheduled for launch in 1992, will explore the surface of the planet Mars for 1 Martian year. One of the scientific instruments on-board the spacecraft will be a gamma-ray spectrometer (GRS) that will utilize a coaxial n-type HpGe detector. The GRS shall make high-resolution energy measurements of gamma rays emitted by the planetary surface. Cosmic-ray bombardment of the planetary surface induces gamma-ray emission due to subsequent primary and secondary nuclear interactions. Gamma-ray measurements made aboard the polar orbiting Mars Observer spacecraft can be used to infer chemical composition of the Martian surface.

Previous experiments [1] and flight experience [2] have indicated that HpGe detectors exposed to cosmic radiation can suffer significant radiation damage. As a result, the energy resolution of the HpGe detector will degrade to such a degree that it is not useful for further measurements.

The purpose of this experiment was to obtain more detailed information on the behavior of HpGe detectors under irradiation with high-energy charged particles in space and to test methods of annealing radiation-damaged HpGe detectors in a closed system. Basic scientific as well as engineering data on detector performance under simulated space exposure and operating conditions were collected. These data will be used to help in the design, control, and understanding of how to maintain the health of HpGe detectors during future space missions.

Several HpGe detectors were exposed to a proton irradiation at the French accelerator facility Saturne (Laboratoire National Saturne, Saclay). One detector was a flight-type version of the Mars Observer gamma-ray HpGe detector with a volume of 130 cm^3. Six other HpGe detectors having volumes of 90 cm^3 were grouped in pairs, each pair mounted in a special double-cryostat. Each pair consisted of a n-type and a p-type germanium crystal.

Simulation calculations on the interaction of protons with germanium were carried out by using the HERMES code system. Implications from the calculations and space environment conditions led to special requirements for the proton beam and detector setup. At the accelerator a 1.5-GeV proton beam with a cross sectional area of 20 cm in diameter and with an intensity distribution of less than 20 % variation was obtained. The proton flux was as low as about 10^5 protons $cm^{-2}sec^{-1}$ and was measured with plastic scintillation counters and monitor foils. The HpGe detectors were arranged inside the beam cross section in such a way that no Ge crystal was in the geometrical shade of another. By using a special heating device the detectors were held at operating temperatures of 90 K, 100 K, and 120 K to cover a temperature range expected for a planetary mission. The irradiation of the detectors occurred in several steps until an accumulated fluence of about 10^8 protons cm^{-2} was reached. The detectors were irradiated in predetermined increments of proton fluence. During irradiation interruptions, gamma-ray spectra of ^{60}Co were taken to evaluate the performance of the detectors as a function of accumulated charged particle fluence.

At completion of the irradiation, all detectors were characterized and cooled stepwise to LN_2 temperatures. Then, the detectors were transported in special containers to the laboratory at Mainz, where a detailed characterization of their performance was carried out.

A total proton fluence of 10^8 protons cm^{-2} is about equivalent to one year of exposure in space. At elevated temperatures the observed energy resolution degradation after accumulation of

this fluence would not allow for high-resolution gamma-ray spectroscopy. But, as shown later, annealing can remove the damage.

During the stepwise irradiation, the peak shape of the n-type detectors showed a significant change. Before the irradiation the shapes were either pure Gaussian or showed a little exponential tailing at the low-energy side. During the irradiation the exponential tailing evolved until it dominated the entire low-energy side of the the peak. A Gaussian shape was maintained at the high-energy side. More irradiation produced a new feature depending on the operating temperature: a broad Gaussian peak sitting on top of the exponential tailing (in a logarithmic display visible as a bump).

The full-width-at-half-maximum (FWHM) of the three 90-cm^3 n-type detectors is shown in Figure 1 as a function of proton fluence and operating temperature. The detector held at 90 K showed the best resistance against degradation of energy resolution. The detector held at 100 K (further on called "Yellow") exhibited an increase of degradation to 6 keV after being exposed to a fluence of 1.1×10^8 protons cm^{-2}; prior to the irradiation the resolution was 2.1 keV at 100 K. At an accumulated fluence of 6×10^7 protons cm^{-2}, which corresponds to about a half year of exposure in space, the energy resolution of detector Yellow was still below 3 keV. After the irradiation detector Yellow was cooled down to 90 K and its FWHM improved to 4.5 keV. The detector at 120 K showed an almost linear dependence of FWHM vs. fluence in contrast to the curve of Yellow, which led to an resolution degradation from 2 keV before the irradiation to 3 keV at an accumulated fluence of 3×10^7 protons cm^{-2}.

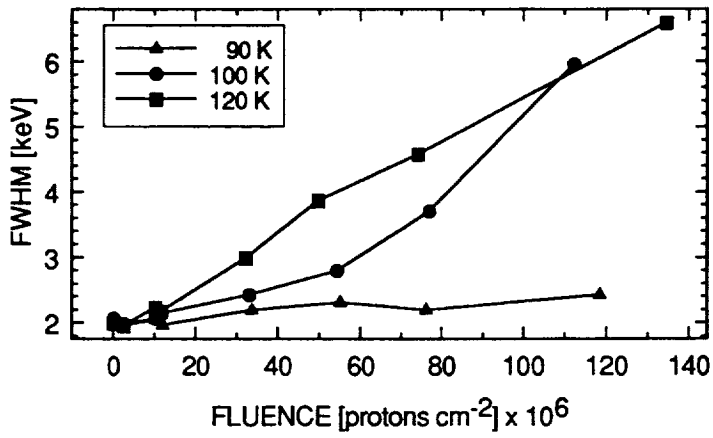

Fig.1 FWHM of the 1.3-MeV line of ^{60}Co for 3 n-type HpGe detectors at different temperatures as function of proton fluence.

Temperature cycling of damaged detectors between a reference temperature of 90 K and temperatures up to 130 K proved that irreversible additional loss in detector performance occurred above 120 K. For detector Yellow, it was observed that between 125 and 130 K an irreversible increase of damage occurred, *i. e.* if the detector was cooled down to 90 K after being at 130 K, its energy resolution had increased to 6.7 keV compared to 4.5 keV at 90 K. Heating up to room temperature produced only a small further increase of the resolution degradation (7.2 keV at 90 K).

During annealing (heating up to 100°C or higher) the detectors stayed in their special designed cryostat (the Ge crystal was encapsulated in a vacuum-tight inner can). After having annealed detector Yellow at a temperature of 105°C for 11 hours, almost all damage was removed (resolution improved from 7.2 to 2.4 keV). Further annealing of 50 hours at the same temperature brought the energy resolution back to its original value. A further indication of complete recovery of the annealed detector was the lack of variation in the intrinsic detector energy resolution as a function of temperature in the range 90 K to 120 K.

The irradiation and annealing cycles of the detectors simulated space exposure and operating procedures as closely as possible. The annealing temperatures applied to the detectors are available on the Mars Observer GRS. The study showed that HpGe detectors can successfully be used in long-term space experiments.

References: [1] Pehl R.H., Madden N.W., Elliott J.H., Raudorf T.W., Trammell R.C., and Darken L.S. (1979) IEEE Trans. Nucl. Sci. NS-26, 321-323. [2] Mahoney W.A., Ling J.C., and Jacobson A.S. (1981) Nucl. Instr. Meth. 185, 449-458.

CHEMICAL EVOLUTION AND OXIDATIVE WEATHERING OF MAGMATIC IRON SULFIDES ON MARS

Roger G. Burns and Duncan S. Fisher, Department of Earth, Atmospheric and Planetary Sciences, Massachusetts Institute of Technology, Cambridge, MA 02139

INTRODUCTION. Ferric-bearing phases in the martian regolith testify to oxidative weathering reactions near the surface of Mars. A paragenetic link between primary magmatic sulfide minerals on Mars and their weathering products (gossans) has been proposed by us [1-3]. This model is based on petrogenetic associations between komatiitic rock-types, Viking geochemical data, SNC meteorites, and terrestrial magmatic sulfide ore deposits [4]. It appears that unique conditions during the evolution of the martian crust have conspired to generate an acidic groundwater (permafrost) environment that has facilitated chemical weathering of basaltic rocks on Mars.

Some of the steps that have been proposed during oxidative weathering of iron sulfides [1-4] are summarized by reactions formulated in Table 1. Initially, deep-weathering reactions involving dissolved ferric iron in acidic groundwater percolating from the surface converts pyrrhotite to pyrite (reaction {1}). Pyrite is then oxidized either by ferric ions {2} or by groundwater equilibrated with oxygen in the atmosphere {3}, even under an oxygen partial pressure of 10^{-5} bar existing in the present-day martian atmosphere. Strongly acidic (pH 1 to 5) and sulfate-rich solutions are generated which stabilize and mobilize a variety of simple and complex ions of Fe, including Fe^{2+}, Fe^{3+}, $FeSO_4^+$, $FeOH^{2+}$, etc. Above the water table, these dissolved ions become unstable and produce hydronium jarosite {4} or eventually goethite by further oxidation {5}, hydrolysis {6}, and decomposition {7} reactions, each of which liberates H^+ ions thereby promoting chemical weathering of basaltic silicate minerals {8}.

To test this weathering model, komatiitic pyrrhotites and olivines have been exposed to sulfuric acid solutions, with and without the addition of ferric iron to simulate deep-weathering processes. We report here measurements made on the reaction products, and summarize tectonic and geochemical processes that might have modified the surface of Mars.

EXPERIMENTAL PROCEDURES. Powdered samples of pyrrhotite (Fe_7S_8) and olivine (Fa_{49}) were reacted in stoppered flasks with sulfuric acid (pH 2) at 60°C, with and without the addition of dissolved 1M ferric sulfate, for time periods ranging from 1 to 5 weeks. Reaction products were filtered, washed with cold distilled water, air-dried and measured by Mossbauer spectroscopy at ambient (295K) and liquid helium (4.2K) temperatures to characterize the X-ray amorphous Fe^{3+}-bearing phases formed in the reactions. Correlative Mossbauer spectra were also obtained for pyrite, marcasite, hematite, goethite, and jarosite. The spectra were calibrated against a metallic iron foil standard.

RESULTS. Examples of 4.2K Mossbauer spectra of pyrrhotite before and after reaction with pH 2 sulfuric acid are shown in Figure 1. The unreacted pyrrhotite spectrum (Fig. 1a) is complex and consists of 3 or 4 superimposed magnetic hyperfine sextets. After reaction with H_2SO_4, additional peaks appear at approx. 0.1 and 0.7 mm s^{-1} (Figs 1b & 1c) attributable to FeS_2 (pyrite or marcasite), which are intensified (Fig. 1c) when $Fe_2(SO_4)_3$ is present as a lixiviant. New peaks also occur near -7.75 and +8.5 mm s^{-1} and represent another component sextet, the magnetic hyperfine splitting parameter of which (H = 50.6T) resembles the value of goethite [5]. The breadth (Fig. 1b) or asymmetry (Fig. 1c) of the two goethite peaks suggest that some hydronium jarosite (H = 49.3T) may also be present in the reaction products. The Mossbauer spectra of reacted pyrrhotites, therefore, indicate that sulfuric acid has induced the pyrrhotite → FeS_2 (pyrite or marcasite) → goethite (+ jarosite) oxidative reactions formulated in Table 1. Nanophase goethite is also formed during reactions of olivine with H_2SO_4 [4], particularly in the presence of dissolved Fe^{3+} ions, hydrolysis of which is unlikely in acidic (pH 2) solutions.

DISCUSSION. The experimental results for H_2SO_4-degraded pyrrhotites support our proposed model for the oxidative weathering of Fe-S sulfide minerals, in which supergene alteration of pyrrhotite in groundwater and the formation of secondary FeS_2 phases precedes the deposition of goethite and jarosite in gossans above the water table [1-4]. Dissolved Fe^{3+} ions clearly promote the formation of supergene pyrite or marcasite, and the acidic groundwater causes chemical weathering of ferromagnesian silicates such as olivine to nanophase goethite. Similar oxidative weathering reactions involving pyrrhotite and olivine in komatiitic basalts are suggested to have occurred on Mars, contributing to the ferric-bearing materials present in the regolith there.

EVOLUTION OF THE MARTIAN SURFACE. Oxidative weathering of sulfides on Mars has been largely confined to pyrrhotite, perhaps associated with pentlandite and minor chalcopyrite, which predominate as accessory minerals in mafic igneous rocks and in associated ore deposits. Partial melting of the martian mantle estimated to contain about 4.5 wt. % S [4] produced iron-rich basaltic magma which

reached the surface of the planet via massive shield volcanoes and as fissure eruptions, transporting high concentrations of dissolved S^{2-} and HS^- to the surface. Extrusion of turbulent low viscosity lava, segregation of immiscible FeS liquids during cooling, gravitational settling and fractional crystallization of sulfide minerals in the lava flows, produced thinly disseminated iron sulfide mineralization over large areas of Mars. Massive ore deposits were also deposited locally at the base of structural depressions or in channels eroded by advancing lava flows [6]. Fracturing associated with this volcanism facilitated deep-weathering reactions by permeating groundwater early in the history of Mars. However, because plate tectonic activity appears to have been insignificant on Mars, the apparent absence of spreading centers and subduction zones has minimized acid-buffering of aqueous solutions by wall-rock alteration. Therefore, the acidity of groundwater, now permafrost, has been maintained during the chemical evolution of the martian surface, aiding the chemical weathering of silicates in the basaltic crust when water is present. Furthermore, since tectonic-induced interactions of martian mantle with crust, hydrosphere and atmosphere have been minimal, sulfide mineralization has not evolved on Mars beyond pyrrhotite-pentlandite assemblages associated with mafic igneous rocks. Therefore, common terrestrial ore deposits such as porphyry copper and molydenum, granite-hosted mineralization, and sediment-hosted galena-sphalerite assemblages [7] have not formed on Mars.

REFERENCES. [1] R.G.Burns, *Proc. 17th LPSC, JGR*, 92, E570 (1987); [2] R.G.Burns, *Proc. 18th LPSC*, 713 (1988); [3] R.G.Burns & D.S.Fisher, *LPI Tech. Rept., 88-05* 34 (1988); [4] R.G.Burns & D.S.Fisher, *LPI Tech Rept., 89-04*; 20(1989); [5] E.Murad & J.H.Johnston, in *Mossbauer Spectroscopy Applied to Inorganic Chemistry* (G.J.Long, ed.; Plenum) 2, 507 (1987); [6] A.K.Baird & B.C.Clark, *Nature*, 311, 18 (1984); [7] C.Meyer, *Ann. Rev. Earth Planet. Sci.*, 16, 147 (1988); [8] Research supported by NASA grants NSG-7604 and NAGW-1078.

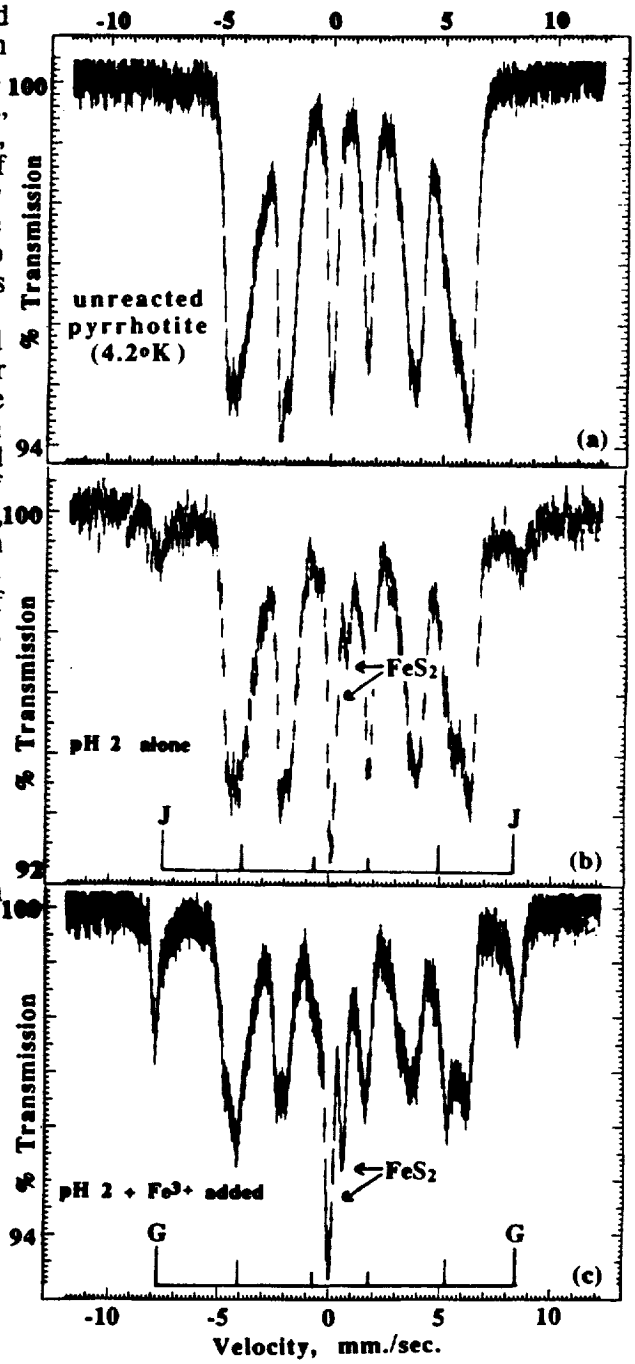

FIGURE 1. Mossbauer spectra measured at 4.2K of pyrrhotite (a) before, and (b,c) after, reaction with pH 2 sulfuric acid for 5 weeks at 60°C, in the absence (b) and presence (c) of dissolved 1M ferric sulfate. Peaks attributed to FeS_2 are identified, as are the positions of the goethite (G) and jarosite (J) sextet spectra

TABLE 1. Chemical weathering reactions of iron sulfides and silicates

{1} $Fe_7S_8 + 6\,Fe^{3+} \Rightarrow 4\,FeS_2 + 9\,Fe^{2+}$

{2} $FeS_2 + 14\,Fe^{3+} + 8\,H_2O \Rightarrow 15\,Fe^{2+} + 2\,SO_4^{2-} + 16\,H^+$

{3} $2\,FeS_2 + 2\,H_2O + 7\,O_{2\,(aq)} \Rightarrow 2\,Fe^{2+} + 4\,SO_4^{2-} + 4\,H^+$

{4} $2\,FeSO_4^+ + FeOH^{2+} + 6\,H_2O \Rightarrow (H_3O)Fe_3(SO_4)_2(OH)_6 \Downarrow + 4\,H^+$

{5} $4\,Fe^{2+} + 6\,H_2O + O_{2\,(aq)} \Rightarrow 4\,FeOOH + 8\,H^+$

{6} $Fe^{3+} + 2\,H_2O \Rightarrow FeOOH \Downarrow + 3\,H^+$

{7} $(H_3O)Fe_3(SO_4)_2(OH)_6 \Rightarrow 3\,FeOOH + 2\,SO_4^{2-} + 4\,H^+ + H_2O$

{8} $(Mg,Fe)_2SiO_4 + 4\,H^+ \Rightarrow 2\,(Mg^{2+} + Fe^{2+}) + SiO_{2\,(aq)} + 2\,H_2O$

MOSSBAUER SPECTRA OF OLIVINE-RICH WEATHERED ACHONDRITES: II. BRACHINA, CHASSIGNY, ALHA 77005, AND NAKHLA

Roger G. Burns and Sondra L. Martinez, Department of Earth, Atmospheric and Planetary Sciences, Massachusetts Institute of Technology, Cambridge, MA 02139.

INTRODUCTION. Olivine predominates in several SNC meteorites believed to have originated from Mars, including Chassigny (approx. 90 modal % $Fa_{31.5}$; **[1]**) and ALHA 77005 (~52% Fa_{28-34}; **[2]**). It is also a significant constituent of Nakhla (15.5% Fa_{68}; **[3]**), and is present in minor amounts in EETA 79001 lithology A, Lafayette and Governador Valadares **[4]**. Furthermore, almost 80% of Brachina is olivine (Fa_{30}) **[5,6]** (which is related to ALHA 84025; **[7]**), and this meteorite was once grouped with the SNC meteorites. Because olivine is particularly reactive in low temperature environments and forms iddingsite under hydrothermal conditions and during weathering **[8]**, the presence of such ferric-bearing oxyhydroxide and phyllosilicate assemblages may be indicative of oxidative weathering in an aqueous environment on Mars. Since the presence of ferric iron in amounts exceeding 1-2% is usually readily detectable by Mossbauer spectroscopy **[9]**, and because preliminary measurements of weathered meteorites at very low temperatures enabled nanophase hydrated Fe(III) oxide phases to be identified **[9,10]**, we have measured the spectra of several olivine-rich achondritic meteorites and report here 295K and 4.2K Mossbauer spectral data for SNC and related meteorites; an accompanying abstract **[11]** describes similar measurements on a suite of ureilites found in Antarctica.

SPECIMENS STUDIED. Achondrites acquired for the Mossbauer spectral measurements included: ~100 mg chips from interior portions of Brachina, Chassigny and Nakhla; homogenized powders from the Antarctic Meteorite Collection of the "dark" (olivine-rich) and "light" (olivine-depleted) fractions of ALHA 77005; and a powdered eucrite (ALHA 80102) showing moderate rustiness, which served to locate pyroxene peaks in the low-temperature spectra. Experimental details are described in the accompanying abstract **[11]**

RESULTS. Assembled in Figure 1 are the 4.2K Mossbauer spectra of the six achondrites. It is immediately apparent from Figure 1 that peaks at approx. -7.75 and +8.5 mm s^{-1} are most conspicuous in the Brachina spectrum (Fig. 1a), yielding a value of 50.3T for the magnetic hyperfine field which corresponds to values for goethite. Magnetic ordering of this Fe(III) oxyhydroxide phase is not observed in the 295K spectrum, however, indicating that the ~7% ferric iron present in Brachina occurs as nanophase (<10 nm) goethite. Very weak FeOOH features appear in 4.2K Mossbauer spectra of Nakhla (Fig. 1e) and eucrite ALHA 80102 (Fig. 1f), but not in the spectra of Chassigny (Fig. 1b) or the ALHA 77005 "dark" (Fig. 1c) and "light" (Fig. 1d) fractions, even though the 295K spectra resolved small amounts of ferric iron in Chassigny (2.3% Fe^{3+}) and ALHA 77005 (1.7% Fe^{3+}; **[10]**) as well as Nahkla (1.6% Fe^{3+}; **[9]**). The ferric iron in Chassigny appears to be accomodated in the olivine structure as it is in ALHA 77005 **[12]**, and not in the iddingsite FeOOH phase present in Nakhla and Brachina.

DISCUSSION. The presence of goethite in Brachina correlates with the "small amount of limonite produced by terrestrial weathering" reported when the meteorite was found in South Australia **[5]**. Similar terrestrial weathering could not have occurred in Chassigny and Nakhla which were collected as *falls*, so that their ~2.0 Fe^{3+} probably represents preterrestrial oxidation during exposure on Mars. We also conclude that the ferric iron measured in olivine-separates **[12]** and bulk samples **[9]** of ALHA 77005 did not originate in Antarctica but was produced during low temperature alteration reactions on the martian surface.

REFERENCES. **[1]** R.J.Floran *et al.*, *GCA*, 42, 1213 (1978); **[2]** H.Y.McSween Jr *et al.*, *Science*, 204, 1201 (1979); **[3]** T.E.Bunch & A.M.Reid, *Meteoritics*, 10, 303 (1975); **[4]** H.Y.McSween Jr, *Rev. Geophys.*, 23, 391 (1985); **[5]** J.E.Johnson *et al.*, *Rec. Sth. Austral. Mus.*, 17, 309 (1977); **[6]** C.E.Nehru *et al.*, *Proc. 14th LPSC, JGR*, 88, B237 (1983); **[7]** P.H.Warren & G.W.Kallemeyn, *Proc. 19th LPSC*, 475 (1989); **[8]** R.A.Eggleton, *Clays & Clay Min.*, 32, 1 (1984); **[9]** T.C.Solberg & R.G.Burns, *Proc. 19th LPSC*, 313 (1989); **[10]** R.G.Burns, *Lunar Planet. Sci.*, XX, 129 (1989); **[11]** S.L.Martinez & R.G.Burns, *Lunar Planet. Sci.*, XXI, this vol. (1990); **[12]** R.Ostertag *et al.*, *EPSL*, 67, 162 (1984); **[13]** Research supported by NASA grants NSG-7604 and NAGW-1078.

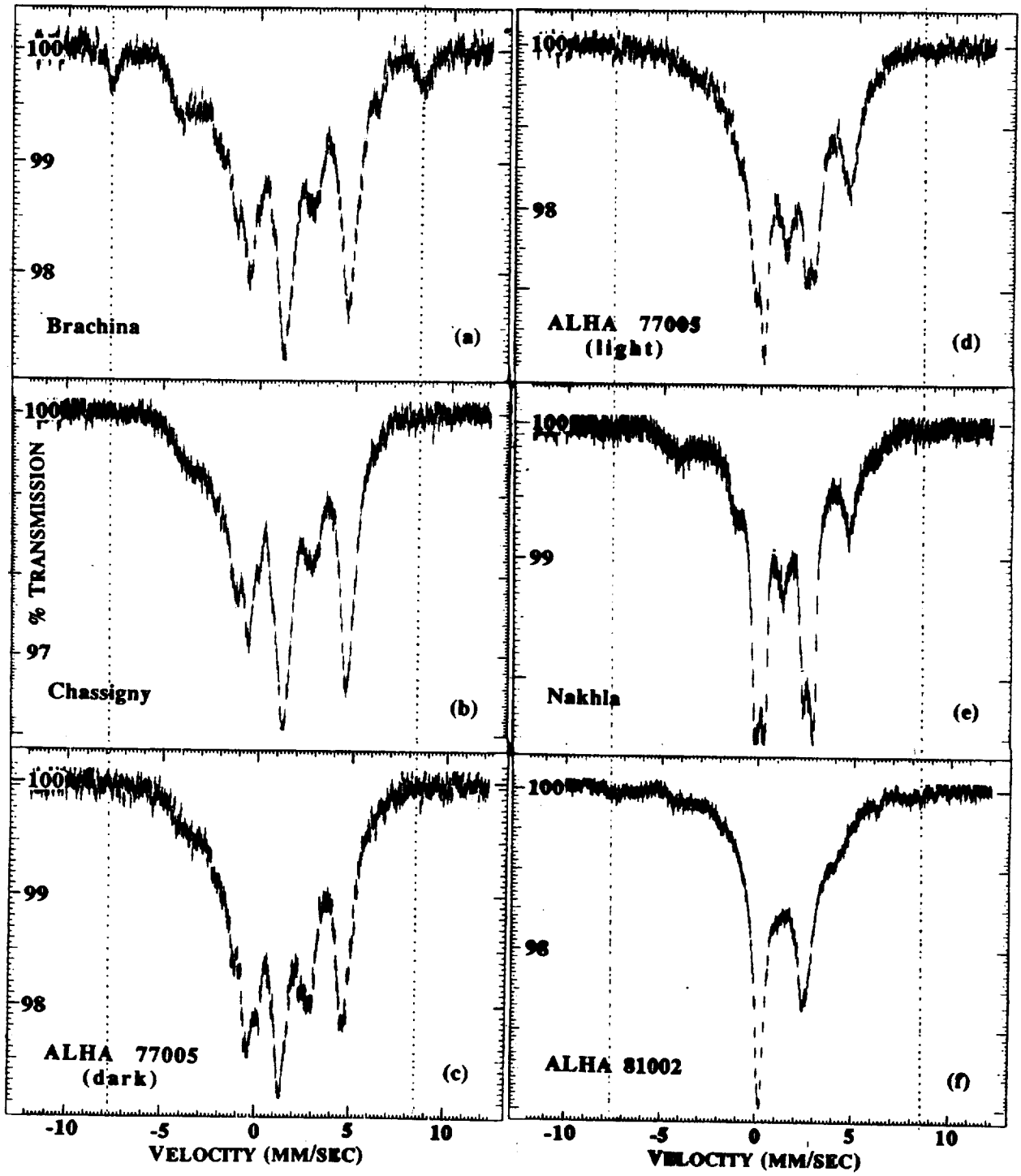

FIGURE 1. Mossbauer spectra measured at 4.2K of a variety of achondrites. (a) Brachina; (b) Chassigny; (c) shergottite ALHA 77005 "dark" (olivine-enriched) and (d) "light" (olivine-depleted) fractions; (e) Nakhla; and (f) eucrite ALHA 81002. Vertical dotted lines indicate the locations of the outermost peaks of the goethite sextet Mossbauer spectrum. This ferric oxyhydroxide phase is present in Brachina, Nakhla and eucrite ALHA 81002. Ferric iron occurring in the olivines, which is resolved in the 295K Mossbauer spectra of Chassigny and ALHA 77005, is obscured by peaks representing the onset of magnetic ordering of ferrous iron.

PHYSIOGRAPHIC CHARACTERISTICS OF MARTIAN DRAINAGE BASINS. CABROL, N.A , Lab.Geo.Phys.(UA0141CNRS) and Lab.Phys.Syst.Solaire.Meudon 92195.-France-

In this study, a martian drainage basin is defined by the limit with the environment of a system of thalwegs. These systems are widly distributed on the craterized uplands and display various morphologies and sizes (from 2000 km^2 to 50 000 km^2). A conceptual model, built up with geometrical data from the 1: 2.000.000 maps, yields to a classification of drainage basins. This classification is based upon the relationship between the perimeter (P) and the area (A) of the basin, and is expressed by two coefficients : *Kd* (drainage density) = $\Sigma Li/A$, where ΣLi is the sum of the basin branch lengths. *Kc* (drainage basin compacity, Gravellius coefficient) = $P/2\pi\sqrt{A}$ # $.28P/\sqrt{A}$. P is the length of a drainage basin limit, which is defined in this method by a line located 10 km upstream the headwater system and including the branch systems until the outlet. This 10 km value considers the limited Viking resolution, and the limit of the hydrogeological system of underground water reservoirs. To test this model, 15 well preserved drainage basins are selected between -47° and +19°Lat. in order to cover a representative distribution. The model is calibrated by 8 terrestrial basins, located on 3 different geological units (Bassin Aquitain, Bassin de la Durance and Bassin de la Seine -France-), respectively in 3 rainfall regimes. These coefficients Kc and Kd characterize the basin physiographies. Within the model, a discriminant parameter Kd/Kc = D (drainage intensity) is established. Terrestrial Kc values vary from 1 to 1.5 and Kd from .02 (karsts : scarcely branched areas) to 300 (badlands, high drainage intensity areas). So, terrestrial D is included between 200 (high drainage intensity) and .01(low drainage intensity) with medium compacity value of 1.5. The relationship between Kd and Kc allows to classify martian and terrestrial basins (Fig.1) which are represented on the graph by their parameters Kd and Kc. Three concentrations appear, one for the terrestrial examples, and two for the martian basins. The gravity center for the terrestrial examples is Kd= .05 and Kc= 1.3, so D=.04. For the martian lower concentration I, the gravity center coordinates are : Kd=.1 and Kc=1.6, so D=.06. For the martian concentration II, the gravity center coordinates are : Kd=.05 and Kc=3, so D=.01.The D martian values for the 15 tested basins are closer to the representative value of terrestrial low drainage basins intensity located on geological units of karstic types. The martian drainage basins of $(5^+/-2)$ $.10^6$ km^2 correspond to a high compacity value and a low thalweg distribution.Martian drainage basins of $(30^+/-10).10^6$ km^2 correspond to a low compacity value and a low thalweg distribution.

A first conclusion is that Kd value varies only between .03 to .15 (Earth .02 to 300). The result is calibrated with 30 other drainage basins on Mars. Because Kd is related to the geological type of the basin, this result indicates a probable undiversified substratum on a wide area (-50°, +10°Lat.) in which local singularities might lead to groundwater occurrences. A second conclusion is : for martian drainage basins, Kc appears as a clear discriminant coefficient.

These conclusions are then correlated with a mapping of headwater branch densities (order 1) on the entire martian surface. The results vary from 100 to 1 per 10^6 km^2, implying a wide interval of variation. These headwater systems are found mainly in the Margaritifer Sinus, Sinus Sabeus, and Iapygia regions. Their dispersion is unconsistant with an organized meteorological feeding origin and with true surface drainage basins. The .03 mean Kd value and the 1.6 to 3 Kc values (corresponding to elongated basins with isolated headwater systems) lead to support the seepage hypothesis.

PHYSIOGRAPHIC CHARACTERISTICS OF MARTIAN DRAINAGE BASINS. CABROL,N.A.

The third conclusion is : the limits of martian drainage basins are not divides. The basins are not joined, they are widely spreaded as relatively small units on wide areas. The methodological hypothesis considering these basins as isolated systems is consistant with the observation.

REFERENCES : Abrahams, A.D, 1984 Channels networks : a geomorphological perspective. Water.Res.Research, **20**, p161-188. Baker, V.R, and Partridge, J.B, 1986 Small martian valleys : Pristine and degraded morphology. J.G.R 91, p3561-3572. Battistini, R, 1985, in Klinger et al (eds), Hydrolithosphere and problem of subsurface ice in equatorial zone of Mars, Ices in the Solar System, p607-617. Cabrol, N.A, 1988, Compte-rendu des Journées de Planétologie. (CNRS/INSU). Cabrol, N.A, 1988 Morphological variations and evolution of channels on Mars. LPI, XX, p136-137. Carr, M.H, 1986 Mars a water rich Planet? Icarus **68**, p187-216.

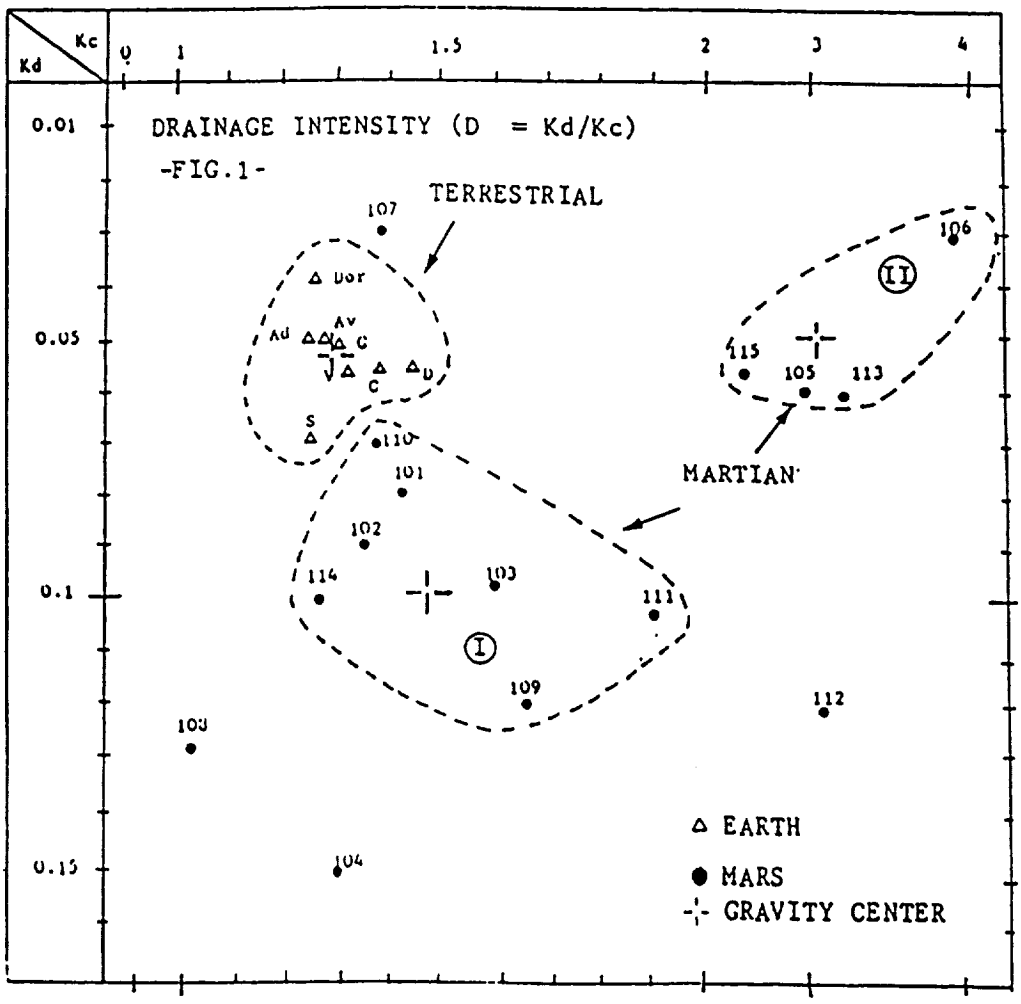

ANALYSIS OF MARINER 6 AND 7 SPECTRA FOR WEAK ABSORPTION FEATURES FROM 2 TO 6 μm, Wendy M. Calvin and Trude V. V. King, U. S. Geological Survey, Denver, Colorado 80225

The current study of the Mariner 6 and 7 spectra was undertaken to identify previously unrecognized absorption features and to confirm the results of recent ground-based observation of Mars by Clark et al. (1989), Blaney and McCord (1989), and Pollack et al. (1989). The Mariner data have the advantage that they are not affected by terrestrial atmospheric absorption, have higher spatial resolution than terrestrial observations, and cover the short wavelength infrared region with reasonably high spectral resolution. However, the Mariner data are subject to a variety of other uncertainties which we have attempted to correct for, in as far as is possible twenty years after the original flyby.

The Mariner 6 and 7 infrared spectrometer data set was obtained from Martin (1985), who provided corrections to the current latitude and longitude system and an initial wavelength calibration. The wavelength region from 2 to 6μm is covered by two halves of a circular variable filter wheel. The first wavelength segment is 1.9 to 3.7μm and the second is 3.0 to 6.0μm. In between each half of the filter wheel is a clear aperture which produces a fiduciary spike ostensibly for wavelength calibration. The use of the fiduciary spikes for this purpose was found to yield inaccurate wavelengths, as did corrections using atmospheric bands at one side of a wavelength segment. Apparently the rotation rate of the filter wheel varied nonlinearly and so adjustments at one side of the wavelength segment often will not accurately predict wavelengths on the other side of the wavelength segment. Further wavelength calibrations were performed using atmospheric CO_2 bands, where available, and fiduciary spikes. In the 3 to 4-μm wavelength region where no strong atmospheric bands occur a feature caused by an absorption in the filter at 3.4μm (Herr et al., 1972, and Pimentel et al. 1974) was used for calibration.

Other corrections made to the data set include removal of a space background signature, correction for the instrument response as a function of wavelength, removal of the thermal flux to the reflected component and finally correction of the reflected solar response to reflectance. These additional corrections were only made for the 3 to 6-μm wavelength region because at shorter wavelengths the space background did not vary significantly from zero and calibration spectra are not yet available to derive accurate instrument response functions. For the longer wavelength segment space background responses were determined from 6 spectra recorded after the flyby. The average of these was fairly noisy and it was necessary to smooth the response function using a fast Fourier transform. Instrument response functions, determined from black-body calibration spectra included in the flight data set, were also smoothed to eliminate the introduction of noise. In addition, the solar flux was calculated and adjusted for Mars' distance from the sun, and the thermal contribution was calculated using temperatures determined by the original instrument team (Pimentel et al., 1974).

In the wavelength region from 1.9 to 3.6μm, several absorption features that cannot be attributed to atmospheric absorptions are observed in the processed Mariner 6 and 7 data. The most dominant feature is the broad 3μm

absorption associated with hydrated surface minerals which was discussed by Pimentel et al. (1974). An absorption feature is also observed in the 2.3 to 2.4-μm wavelength region which is in agreement with the Clark et al. (1989) observations. However, the resolution of the instrument is insufficient to verify whether the 2.3-2.4μm feature is atmospheric or mineralogic in origin. Between approximately 2.45 and 2.62μm there are two broad absorption bands. The shorter of the two bands is centered on 2.48μm and seems to be correlated to a band observed by Clark et al. (1989) at 2.45μm. The 2.48μm absorption feature in the Mariner data could be shifted in wavelength because the wavelength calibration is fixed at isolated points, the closest of which is at 2.7μm. The second band is broader (2.5- 2.65μm) and can possibly be explained by discrepancies between the amount of atmospheric water modeled and observed or the presence of hydrated surface minerals. Removal of the atmospheric signature in the 2.7 to 2.8-μm region indicated a residual absorption feature at 2.76μm which can be attributed to the presence of OH-bearing mineral phases. This feature can be seen weakly in some of the original Mariner 7 spectra. Attempts to confirm it with Mariner 6 were unsuccessful as the signal to noise ratio of Mariner 6 data is much worse than that of Mariner 7. Uncertainties associated with removing atmospheric absorptions have precluded a definitive identification of an OH-absorption feature.

In the 3 to 6-μm region the strongest absorption features result from atmospheric absorptions. However, a broad 3-μm absorption associated with hydrated minerals is present. The 3.8-μm feature reported by Blaney and McCord (1989) is confirmed. Over Hellas the 3.8μm feature is nearly twice as deep as is predicted for a four airmass atmosphere, indicating a mineralogical as well as atmospheric origin. In addition, a weak feature at 5.35μm, on the edge of the atmospheric CO_2 band at 5.2μm, is observed in both Mariner 6 and Mariner 7 spectra of the Meridiani Sinus region. These absorption features can result from the presence of OH-bearing mineral species and possibly, based on preliminary laboratory spectra, from S-bearing mineral phases or a combination of the two mineral species.

This study confirms the presence of several weak absorption features observed by terrestrial observations and identifies previously unrecognized absorption features in the wavelength regions from 2.5 - 2.65 and 5.35μm in Mariner 6 and 7 data. These features appear to be mineralogic rather than atmospheric in origin and are believed to result from the presence of OH- or S-bearing minerals on the Martian surface.

REFERENCES

Blaney and McCord, submitted to *J. Geophys. Res.*, 1989. Clark, Swayze, Singer and Pollack, submitted to *J. Geophys. Res.*, 1989. Crisp, submitted to *J. Geophys. Res.*, 1989. Herr, Forney, and Pimentel, *Appl. Opt.*, 493-501, 1972. Martin, Mariner 6 and 7 data released under the Pilot Planetary Data System, 1985. Pimentel, Forney, and Herr, *J. Geophys. Res.*, 1623-1634, 1974. Pollack et al., *Eos*, *70* 1171, 1989.

THE EFFECTS OF FLOODS, VOLCANISM AND POLAR PROCESSES ON THE D/H RATIO IN THE MARTIAN ATMOSPHERE. M. H. Carr, U. S. Geological Survey, Menlo Park, CA 94025.

Water in the martian atmosphere is 5.1 times more enriched in deuterium than terrestrial water (Owen et al., 1988; Bjoraker et al., 1989). The enrichment has been previously attributed to either massive loss of water early in the planet's history (Owen et al., 1988) or to the presence of only a very small reservoir of water that has exchanged with the atmosphere over geologic time (Yung et al. 1988). However, early massive loss of nearly all the planet's water appears inconsistent with abundant evidence for the action of water throughout Mars history, and exchange of only small amounts of water with the atmosphere is contrary to interpretation of channels as water worn, and interpretation of the poles as a sink for water. Here we examine what effect geologic processes might have on D/H in the atmosphere, and assess whether the geologic model for the evolution of the Mars surface that has been developed over the last two decades needs major revision.

Outflow channels are generally believed to have been formed by large floods. A large flood would immediately inject a substantial amount of water into the atmosphere, then in the long term water would sublime into the atmosphere from the ice rich deposits that must have formed where the water pooled after the flood was over. To estimate the amount of water injected into the atmosphere, a flood was divided into three stages. Assuming present conditions on Mars at the time of a flood, and using previously derived techniques for determining sublimation rates (Toon et al., 1980), it was estimated that roughly 10^{17} g of water would evaporate into the atmosphere in the active stage, while the flood was in progress. This water probably would have frozen out rapidly at the poles to form an ice layer a few centimeters thick. In the second stage, the lake that formed at the end of the flood channel freezes, and the thermal anomaly created by the presence of the lake dissipates. It was estimated that in a typical flood the terminal lake would take about one year to freeze solid and the thermal anomaly would take about 6 years to dissipate during which time about another 10^{17} gm of water would evaporate into the atmosphere and be precipitated out at the poles. The long term fate of the terminal ice deposits would depend on their latitude and thickness of any superimposed dust. Most of the floods in Elysium and Hellas, and around Chryse Planitia appear to have pooled at high latitudes (McGill, 1985; Lucchitta et al., 1986). Dust would affect the stability of ice deposits by reducing daily temperature excursions and inhibiting movement of water vapor from the buried ice to the surface. These effects were modelled using the techniques developed by Clifford and Hillel (1983). For an ice deposit at 50^{o} latitude, covered with a few tens of centimeters of dust, sublimation rates are estimated to be extremely low, in the range of 10^{-7} - 10^{-8} g cm^{-2} yr^{-1}. Sublimation rates at the equator are over 100 times higher. Thus, the immediate effect of a flood on the atmospheric D/H would be to reset the atmospheric D/H to the value for groundwater. The long-term effect would depend on the latitude of the terminal ice deposit. Sublimation rates are so low for high latitude deposits that the D/H in the atmosphere could become enriched with respect to groundwater in response to upper atmosphere losses. If the terminal ice deposit were at low latitude, the atmosphere would be maintained at the D/H value for groundwater until the deposit had fully sublimed.

D/H ON MARS
Carr, M. H.

Volcanism is likely to have episodically introduced water into the atmosphere throughout the history of the planet. Greeley (1987) estimates that 25 to 41 m of water averaged over the whole planet have been introduced onto the surface by volcanism during the last 3.5 Ga. Judging from the size of lava flows, individual eruptions could almost instantaneously introduce 10^{13} to 10^{17} gm of water into the atmosphere. The larger eruptions would inject enough water into the atmosphere to reset its D/H ratio to that of juvenile water. Much of the erupted water would have rapidly frozen out at the poles without having its D/H ratio changed.

The effect of polar processes on D/H in the atmosphere depends on how actively water at the poles is exchanging with the atmosphere. If the Yung et al. (1988) estimates of loss of hydrogen from the upper atmosphere are correct, and water at the poles has actively interchanged with the atmosphere, then the poles can contain no more than 0.2 m of water averaged over the whole planet. But this conclusion is inconsistent with evidence of introduction of water onto the surface by floods and volcanism, and with the current perception of the polar layered terrains as ice rich. Jakosky (in press) suggested that Yung et al (1988) had underestimated hydrogen loss rates. He suggested that loss rates at high obliquity could be 100 times present rates, and the time averaged value 20 times the present rate. If so, then the reservoir of water at the surface would be correspondingly increased. An alternative explanation of the inconsistency is that exchange of water between the poles and the atmosphere is minimal, and restricted to the upper few centimeters of the polar deposits. Thus, new ice added to the polar deposits as a result of floods or volcanism, retains its initial D/H ratio except for the upper surface. In this case, the D/H in the atmosphere evolves almost independently of the poles, and reveals little about the inventory of water at the surface. Such a scenario is consistent with the crater ages of Plaut et al. (1989), which suggest that the polar layered terrains are older than formerly thought.

We can conclude that the D/H enrichment of the atmosphere is not necessarily that of the bulk of the near surface water. The evolution of D/H in the atmosphere is likely to have been episodic. Floods and eruptions would have periodically reset the atmospheric D/H to the groundwater and juvenile values respectively. Between these events the atmosphere would have become enriched in deuterium at a rate dependent on the rate of interchange of water between the atmosphere and other surface reservoirs such as the poles.

REFERENCES. Bjoraker, G. 1., Mumma, M. J., and Larson, H. P., Proc. 4th Int., Conf. on Mars, Tucson, 69-70 (1989). Clifford, S. M., and Hillel, D., J. Geophys. Res., 88, 2456-2474 (1983). Greeley, R., Science, 236, 1653-1654 (1987). Jakosky, B. M., J. Geophys. Res. (in press). Lucchitta, B. K., LPSC XVII, 498-499 (1986). Mc Gill, G. E., LPSC XVI, 534-535 (1985). Owen, T., Maillard, J. P., deBergh, C., and Lutz, B. L., Science, 240, 1767-170 (1988). Plaut, J. J., Kahn, R., Guiness, E. A., and Arvidson, R. E., Icarus, 76, 357-377 (1988). Toon, O. B., Pollack J. B, Ward, W., Burns, J. A., and Bilski, K., Icarus, 44, 552-607 (1980). Yung, Y. L., Wen, J., Pinto, J. P., Allen, M., Pierce, K. K., and Paulsen, S., Icarus, 76, 146-159 (1988).

CRATER MORPHOLOGY VARIATIONS IN THE ELYSIUM REGION: IMPLICATIONS FOR ICE DISTRIBUTION ON MARS

Julie A. Cave, U.L.O. Planetary Image Centre, 33–35 Daws Lane, Mill Hill, London NW7 4SD.

INTRODUCTION: Variations in crater morphology are attributed to differences in target strength, depth of excavation, presence of near-surface volatiles, and environmental conditions (1,2,3,4). Rampart craters and other features which may be a result of the presence of sub-surface ice have been observed in the Elysium Volcanic province (5). The aim of this study is to examine the distribution of various crater characteristics and to evaluate the usefulness of crater morphology as an indicator of sub-surface ice.

METHODOLOGY: Preliminary mapping of the region indicated a great complexity of crater morphologies. The study area (155–245°, 15°S–47.5°N) covers a wide range of latitude, altitude, surface type and age and there are therefore several factors that could have contributed to the observed morphological variations. Using mosaics of Viking frames (at a scale of 1:1 250 000) the co-ordinates of each crater over 1.875 km in diameter were digitised. A comprehensive classification scheme was devised that recorded the characteristics of each component of the crater allowing as much detail as possible to be used in the analysis. The characteristics of the craters' morphology recorded include: profile, central features, rim nature (continuous, buried *etc.*), rim condition (fresh, terraced, degraded *etc.*), ejecta type and surface texture (for each component of multiple blanket ejecta), geological unit according to references (6) and (7), and local target nature (*e.g.* lava flow, crater ejecta, channel floor). A confidence factor was also included since the precision of interpretation varied with resolution, although wherever possible the descriptive details were confirmed by checking the highest resolution images available. These details were incorporated into a homogeneous database which can be searched systematically to highlight the dominant factors. Initial analysis has concentrated on average or dominant crater characteristics as a function of latitude, altitude, geological unit, crater diameter and local target nature. The database is nearing completion, and initial observations presented here come from a preliminary analysis of 3060 craters in the Northern Hemisphere.

OBSERVATIONS:

(a) Approximately one third of the selected craters have discernable ejecta blankets. Plots of maximum ejecta diameter versus crater diameter (hereafter abbreviated to EvsΦ) provide an indication of the mobility of the ejecta which is presumed to reflect the degree of fluidisation. The majority of the ejecta documented showed some degree of fluidisation (even for the smallest craters), and *very* few radial ejecta blankets were observed (this may be due in part to the resolution, since radial deposits are harder to detect). If the fluidisation of the ejecta *is* due to the incorporation of subsurface volatiles, then variations in the gradients of EvsΦ reflect *changes* in the state or concentration of volatiles rather than a transition from 'dry' to 'wet' materials being excavated (ignoring possible atmospheric effects).

(b) For most geological units there is a well-defined relationship between ejecta diameter and crater diameter. Many units (although the statistics of some are limited) seem to exhibit significantly higher gradients at larger crater diameters. When all the data are combined the resulting graph is a smooth, rising curve, but the data for several units taken individually exhibit gradient discontinuities. The position of such discontinuities, and the gradients appear to depend on the geological unit. The Elysium lava plains, unit AEL1 have a lower gradient of 2.1±0.2, upper gradient of 3.6±3.6, with an assumed break-point occurring at crater diameter 7km. The lower gradient lies between the gradient for similar-sized craters on Elysium Mons itself (AEL2, 2.0±0.1) and that of the channeled deposits AEL3 which originate from the N.W. flanks of the volcano (gradient = 2.9±0.2). This might suggest a *localised* transfer of volatiles from AEL2 to AEL3 driven by the increased thermal gradient of Elysium Mons. Further evidence of volatile enrichment of units AEL3/4 is provided by the marked concentration of double-ejecta craters in this location (see figure 1).

(c) An initial investigation of EvsΦ has revealed no obvious trend with latitude, except that the previously mentioned relationship breaks down at latitudes greater than about 40° N. Plots of EvsΦ in this region indicate a wide scatter of the data, which may be due to the high concentration of pedestal craters here.

(d) The precise target nature does appear to have influenced the spread of the ejecta: a linear EvsΦ relationship occurs for craters that have impacted other crater rims (despite varied geological locations) and a possible linear trend has been observed for craters on volcanic constructs.

CRATER MORPHOLOGY IN THE ELYSIUM REGION: J. A. CAVE

(e) The location of central features is as shown in Figure 1. The peaked craters are widely distributed on many units, while the pit craters are less frequent and have a more limited distribution. The plot of EvsΦ for these craters indicate similar ejecta fluidities, possibly indicating similar formation conditions. The scarcity of pits may be due in part to the infilling or flooding of many of the larger craters in the sample set.

(f) These observations are currently being checked for statistical accuracy. Altitude, radial distance from Elysium Mons, and estimates of the depth of excavation will also be taken into account. The morphological characteristics of the ejecta will be examined simultaneously with the dimensional data.

The database is a valuable aid in the interpretation of the crater morphology in the area, and will also provide information on the ages and resurfacing histories of the units. This work forms part of a detailed investigation of Elysium in which all possible indications of the presence of ice (craters, channels, chaotic and knobby terrain, volcano eruptive styles) are being assessed. Comprehensive studies of the age, nature and distribution of each ice-related landform will enable further constraints to be placed on the importance, timing and distribution of ice in Elysium. In a future project, the Hellas volcanic region will be investigated using the same technique, allowing comparisons to be made between two volcanic provinces of different ages and geological settings.

REFERENCES: (1) Head J.W., Proc. L.P.S.C. VII 2913–2927, 1976. (2) Carr M.H., Crumpler L.S., Cutts J.A., Greeley R., Guest J.E. and Masursky H., J. Geophys. Res. 82 4055-4065, 1977. (3) Mouginis-Mark P.J., J. Geophys. Res. 84 8011–8022, 1979. (4) Bridges N.T. and Barlow N.S., L.P.S.C XX 105–106, 1989. (5) Mouginis-Mark P.J., Wilson L., Head J.W., Brown S.H., Lynn Hall J. and Sullivan K.D., Earth, Moon, and Planets 30 149–173, 1984. (6) Scott D.H. and Tanaka K.L., Map I-1802-A, U.S.G.S., 1986. (7) Greeley R. and Guest J.E., Map I-1802-B, U.S.G.S., 1987.

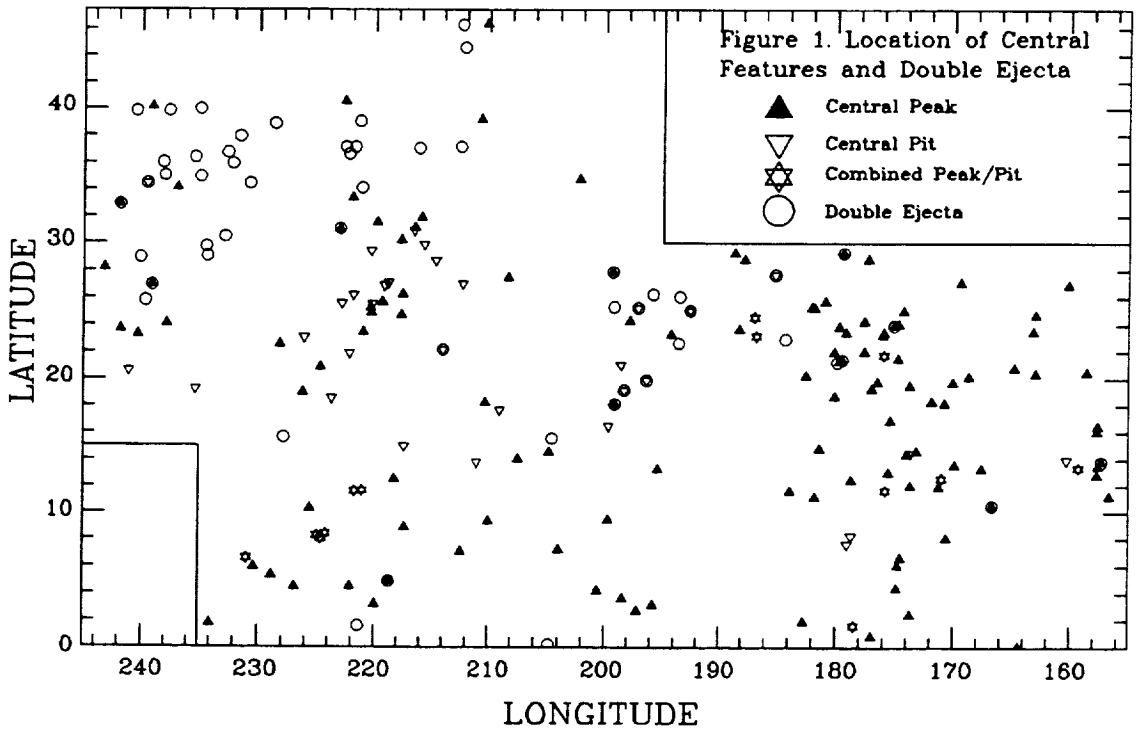

CROSSCUTTING, PERIODICALLY SPACED WRINKLE RIDGES OF HESPERIA PLANUM; D. John Chadwick, Dept. of Geology, Northern Arizona University, Flagstaff, AZ 86001; Thomas R. Watters and Michael J. Tuttle, Center for Earth and Planetary Studies, National Air and Space Museum, Smithsonian Institution, Washington, D.C. 20560

Wrinkle ridges are the long, sinuous anticlinal features which occur on the volcanic plains units of the terrestrial planets and the Moon. Most of these ridges form single, parallel trending groups or concentric patterns within circular basins. The wrinkle ridges of Hesperia Planum on Mars, however, show a much more complex spatial relationship. Two distinct sets of ridges have formed here, crosscutting one another at nearly orthogonal angles, implying a more complex structural history for the region. Termed reticulate ridge patterns (1), these crosscutting ridges are found elsewhere on Mars, but at Hesperia Planum they dominate a very large area to the east and southeast of Tyrrhena Patera.

In this study, the two directional components of the reticulate pattern were separated and ridge spacing was determined using a series of sampling traverses spaced about 20 km apart and oriented perpenducular to the mean ridge trend of both sets. In addition, the two sets of ridges maintain a constant trend over a limited area. Therefore, a large area of Hesperia Planum containing the reticulate pattern was divided into four domains based on the mean trend of the ridges. In each of the domains, the ridge spacings of the two sets were found to be very similar and passed the statistical t-test for equivalency. This test compares two sets of sampled numerical data to determine if they appear to be derived from the same population. The mean spacing for the two ridge sets in each domain are as follows: 38.23 km and 36.13 km for domain one, 32.02 km and 33.75 km for domain two, 36.10 km and 35.58 km for domain three, and 23.80 km and 24.26 km for domain four. The equivalent spacing of both sets of ridges can be explained by two superimposed episodes of buckling at a critical wavelength, governed by the rheological properties and thickness of the plains material in which the ridges formed (2).

The origin(s) of the compressive stresses which formed the reticulate pattern is not readily apparent. The compressional stresses that resulted in the formation of the wrinkle ridges of the Tharsis Plateau may have been in part due to isostatic uplift (3,4,5,6). In the absence of a "Tharsis-like" uplift or load in Hesperia Planum, other mechanisms for the generation of compressional stresses must be found. Compression may have resulted from subsidence due to loading of the volcanic plains material (1), but this mechanism may produce only a single ridge trend related to the shape of the basin. A superimposed regional tectonic event may account for the second ridge set in the reticulate pattern, with local influences accounting for the variable trends of the ridges.

REFERENCES

(1) Raitala, J., Earth, Moon and Planets, 40, 71-99, 1988. (2) Watters, T.R., submitted to JGR, 1989. (3) Banerdt, W.B., M.P. Golombek, and K.L. Tanaka, submitted to Mars, University of Arizona Press, Tucson, AZ, 1989. (4) Banerdt, W.B., R.J. Phillips, N.H. Sleep, and R.S. Saunders, JGR, 87 9723-9733, 1982. (5) Sleep, N.H. and R.J. Phillips, JGR, 90 4469-4489, 1985. (6) Watters, T.R. and T.A. Maxwell, JGR, 91 8113-8125, 1986.

Figure 1. Crosscutting wrinkle ridges of Hesperia Planum; a portion of domain three.

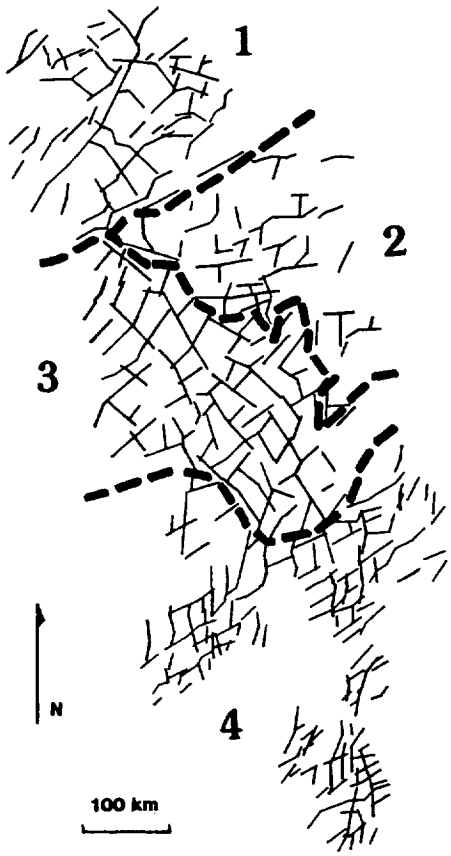

Figure 2. The four domains of eastern and southeastern Hesperia Planum.

GEOLOGIC MAPPING OF LOWER MANGALA VALLES, MARS: EVIDENCE OF FLOODING, SAPPING, DEBRIS FLOW, AND VOLCANISM[1]; Mary G. Chapman and Kenneth L. Tanaka, U.S. Geological Survey, 2255 North Gemini Drive, Flagstaff, AZ 86001.

Two periods of catastrophic flooding are indicated by detailed geologic mapping of the Mangala channel, based on two 1:500,000-scale photomosaics (MTM -05152 and -10151), computer enhancement of Viking images, and photoclinometric channel profiles. The ages of these two episodes are Late Hesperian and Amazonian-Hesperian. Lobate lava flows were erupted during channeling episodes; at least two stratigraphically distinct, resistant lava flows filled the early channels; later flooding eroded the surrounding, less resistant material to leave the lava-capped channels higher than surrounding terrain (i.e. inverted topography). Impact craters that were breached and filled by the earliest phase of flooding formed lakes; some of these ponded areas were covered by lava, others were refilled by the later period of flooding. This flooding period was followed by (1) spring sapping that formed narrow, theater-headed channels (2) debris-flow deposition resulting from chaotic collapse of lava-capped material within breached craters. The direction of drainage was north toward Amazonis Planitia, where the flow materials were partly covered by Middle Amazonian lobate lava flows.

[1]Previously published in GSA Abstracts with Programs, 1989, v. 21, no. 6, p. 4108.

ESA PLANS FOR THE SCIENTIFIC EXPLORATION OF MARS

Chicarro A.F., Space Science Department, ESA/ESTEC, 2200 AG Noordwijk, The Netherlands.

The exploration of Mars by unmanned spacecraft during the last quarter of a century shows that, although geologically less evolved, Mars is far more Earth-like than any other planet. Its internal evolution, resulting in intense tectonic and volcanic activity, and the exogenic processing of its surface, have extended over several billion years. Aside from the Earth, Mars is the only other planet with surface-temperature conditions in the range of stability of complex organic compounds, and therefore, it is an obvious target in the search for present or extinct lifeforms.

Specific goals: The future international exploration of Mars must address major scientific questions, such as: What is the present internal structure, composition and activity of the planet? What are the relative and absolute ages of Mars geologic units? What is the chronology of extensive and compressive tectonic phases? Do SNC meteorites unequivocally come from Mars? What are the most common minerals in volcanic, plutonic and sedimentary rocks? How different were the atmospheric composition, pressure, temperature and dynamics in the past? What is the present surface and subsurface water distribution ? How closely did early Mars resemble the Earth when life appeared on our planet, about 3.8 billion years ago? Are there sediments on Mars containing organic compounds or primitive fossils?

Strategy: ESA has identified three possible areas of European participation in the future international exploration of Mars. These options, two of them dealing with science from the surface, the other addressing science from orbit, are as follows:

• Network science: A network of small surface stations, including a combination of 2 hard landers (surface penetrators) and a cluster of 3 semi-hard landers (mini-probes), thus defining a global/local seismological network (Figure 1) designed for an operational lifetime of one Martian year. The scientific objectives (Table 1) would especially concentrate on the internal structure, mineral and chemical composition, surface meteorology, and entry and descent science measurements. The global/regional network concept could be part of a precursor mission to the *Mars Rover Sample Return* and *Manned Exploration* missions.

• Rover science: A sophisticated sample-acquisition subsystem, including intelligent robotic arm(s) to be placed on-board a rover from another space agency, and capable of stereo-vision, handling, sampling and analyzing rocks and soils. It would conduct detailed in-situ chemical and mineralogical analyses of surface samples, subsurface structural studies, biological experiments, and atmospheric studies, at a number of surface locations within a limited area of mobility. This sampling subsystem could be a contribution to a *Mars Rover Sample-Return* mission.

• Orbiter science: A facility on-board an orbiting spacecraft able to: (i) acquire very high-resolution imagery, (ii) provide radar altimetry and subsurface sounding, or (iii) contribute to the identification of the mineralogical and chemical composition of geologic units. This orbital facility would include a very sophisticated imager or a microwave radar instrument, and would have scientific potential for any surveillance mission of Mars.

International cooperation: Any of the three selected areas for possible European participation would represent a major and independent contribution to a future international mission to Mars, complementing the already scheduled US *Mars Observer* and the USSR's *Mars-94* missions. However, in-depth technical and scientific assessment studies, with emphasis on a *Network mission*, are currently under way in ESA. Following the cooperative path initiated by *Cassini*, a participation in international planetary missions stands as a sensible and viable approach for Europe, in order to take its proper role in the exploration of the Solar System during the next decade and beyond.

Reference: Chicarro A.F. et al., *Mission to Mars: Report of the Mars Exploration Study Team*, ESA SP-1117, European Space Agency, 138 pp., 1989.

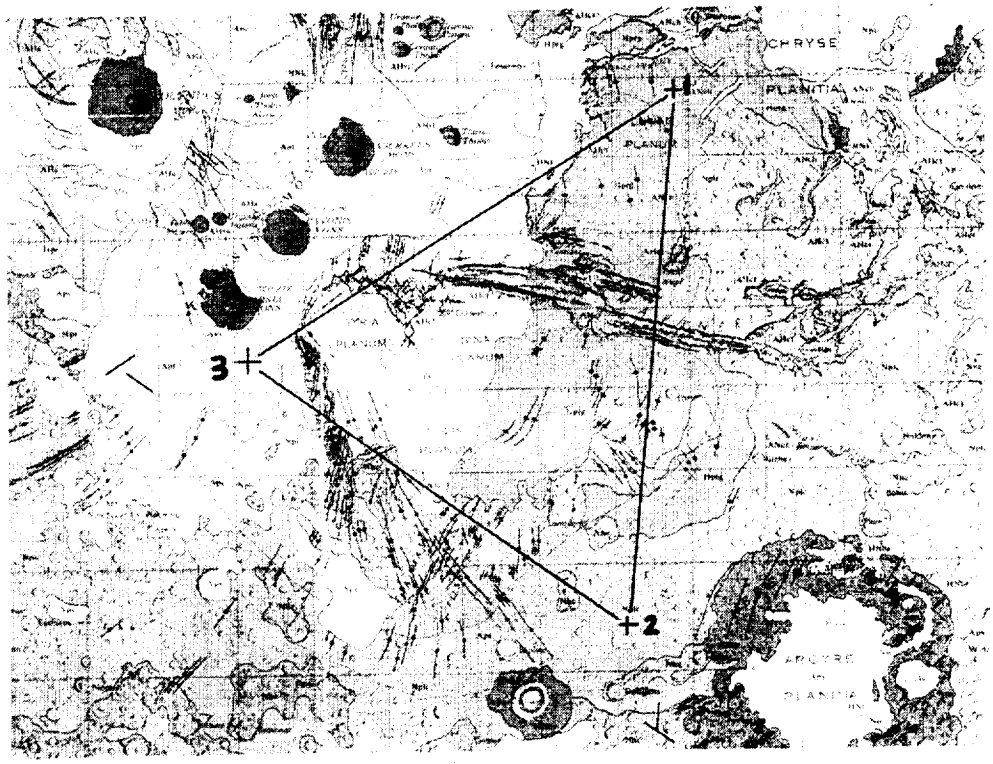

Figure 1: *Location of proposed landing sites in the Tharsis region.*

Site	Device	Payload	Mass	Geochemistry	Scientific interest Meteorology	Seismology
1	Cluster of 3 mini-probes	Total of: 1 global seismometer, 3 local seismometers (1 axis), 3 meteorol. packages, 1 camera, chemical analysis (DEG, TPA, PM, GC)	250 kg including aeroshell and ~5 kg payload on each probe	Analyse ridged plains material and subsurface volatile content	Northern hemisphere site, near Viking Lander-1 in order to compare results	The three sites determine a triangle (of side ~3500 km) which englobes most of the Tharsis uplift and its radial fault system: — likely tectonic activity — good definition of seismic epicentres. Global network: to determine Mars' internal structures Local network: to study the lithosphere's upper layers. In addition, meteoritic impacts do trigger seismic waves: to help determine the planet's internal structure
2	Independently targetted penetrator	For each penetrator: global seismometer (3 axis), camera, meteorol. package, chemical analysis (DEG, TPA, XRF, GRS, GC, PM, CS)	100 kg including ~8 kg payload	Analyse most widespread older unit: complex history of weathering and impacting	Southern hemisphere site: study formation and evolution of global dust storms	
3	Independently targetted penetrator		100 kg including ~8 kg payload	Analyse younger volcanic unit: type of volcanic activity. All three sites have simple geology: unmistakable units	Near the equator and higher-altitude site: study formation of clouds in addition to weather patterns and atmospheric circulation	

Table 1: *Scientific interest of a network of small stations.*

DERIVATION OF MARS ATMOSPHERIC DUST PROPERTIES FROM RADIATIVE TRANSFER ANALYSIS OF VIKING IRTM EMISSION PHASE FUNCTION SEQUENCES;

R.T. Clancy and S.W. Lee, Laboratory for Atmospheric and Space Physics, University of Colorado, Boulder, CO 80309

During the span of the Viking Orbiter missions, several hundred emission-phase-function (EPF) sequences were obtained, in which the IRTM instrument observed the same area of surface as the spacecraft moved overhead. The IRTM data set as a whole is well calibrated, having been corrected for inter-spacecraft, inter-detector, and temporal calibration variations; a conservative estimate for the absolute uncertainty inherent in this data set is 1-2% [1]. The EPF visual brightness observations (passband of 0.3-3.0 μm , effective wavelength of 0.57 μm) present very accurately calibrated albedos of a given region and the atmosphere above it versus emission (and to a lesser extent, incidence) angle. Although these observations were designed for the purposes of surface photometric studies, they are quite suitable for the derivation of atmospheric dust opacities.

We have developed a radiative transfer model of the Mars atmosphere and surface based upon a discrete-ordinates radiative transfer code [2]. Input parameters include the atmospheric dust opacity, the single scattering albedo (ϖ_0) and particle phase function of the atmospheric dust, and the surface bidirectional reflectance. A 16-stream approximation is adopted to adequately represent the model dust and surface phase functions. The surface photometric function is estimated from EPF sequences at low dust opacities and emission angles, where the effects of scattering by atmospheric dust are minimized. The exact behavior of the bidirectional reflectance at large emission angles and/or high dust loading is not critical since the contribution of atmospheric dust scattering dominates the observed reflectance for these regions.

On the basis of an analysis of ~20 separate EPF sequences spanning low and high latitudes, low and high dust opacities, and a wide range of L_S; we find evidence for three distinct aerosol populations. In all three cases it is possible to model the dust scattering with a single dust phase function labelled "IRTM" in figure 1. An empirical phase function representing scattering by non-spherical particles was derived by Pollack et al. [3] to fit the Viking lander observations of dust scattering, and is presented by the solid line in figure 1. The agreement between the "IRTM" and Pollack phase functions is quite good; however the asymmetry factor, g, is 0.55-0.56 rather than the value of 0.79 given by Pollack et al. [3]. A Henyey-Greenstein phase function with g=0.79 is also included in figure 1 to indicate the very large large differences in particle back-scattering implied by g=0.55 versus g=0.79.

We find three separate values of the single scattering albedo, ϖ_0, corresponding to the three aerosol populations. At low-to-mid latitudes for moderate dust opacities (τ = 0.2-1.0), ϖ_0=0.88 fits the EPF observations. Figures 2-4 present a subset of model-data comparisons for this case. At high latitudes (70°-80°N) we find ϖ_0=1.0, indicating that ice clouds are the likely source of particulate scattering. Figure 5b presents a model-data comparison for this case and a best fit attempt with ϖ_0=0.88 (figure 5a). The third aerosol population corresponds to very high dust loading (τ > 2), in which it is necessary to increase ϖ_0 to 0.9-0.92 to fit the data with the "IRTM" dust phase function. Figures 6a and 6b indicate model-data comparisons over Hellas basin in which we attempt to fit the EPF data with ϖ_0=0.88 and ϖ_0=0.92, respectively.

The primary differences between the EPF IRTM and Viking lander derived dust properties are larger ϖ_0 from the EPF analysis (ϖ_0=0.88 versus 0.86) and an increase in ϖ_0 during the peak of the dust storm as found in the EPF analysis (the Viking lander data indicate no such change, J. Pollack, personal communication). It is possible that the distinction of looking from below with lander data and looking from above with the IRTM data may account for these differences. Finer dust (higher ϖ_0 and more backscattering) may be mixed to higher altitudes and may increase during the peak of the dust storms (J. Bergstrahl, personal communication). The downward-looking geometry of the EPF sequences would be more sensitive to a high-altitude, fine component.

This research was supported under NASA Planetary Geology grant NAGW 1378.

REFERENCES: [1] Pleskot, L.K., and E.D. Miner (1981). Time variability of martian bolometric albedo. *Icarus 45*, 179-201. [2] Stamnes, K., S.C. Tsay, W. Wiscombe, and K. Jayaweera (1988). A numerically stable algorithm for discrete-ordinate-method radiative transfer in scattering and emitting layered media. *Appl. Opt., 27*, 2502-2509. [3] Pollack, J. B., D. S. Colburn, F. M. Flasar, R. Kahn, C. E. Carston, and D. Pidek (1979). Properties and effects of dust particles suspended in the martian atmosphere. *J. Geophys. Res., 84*, 2929-2945.

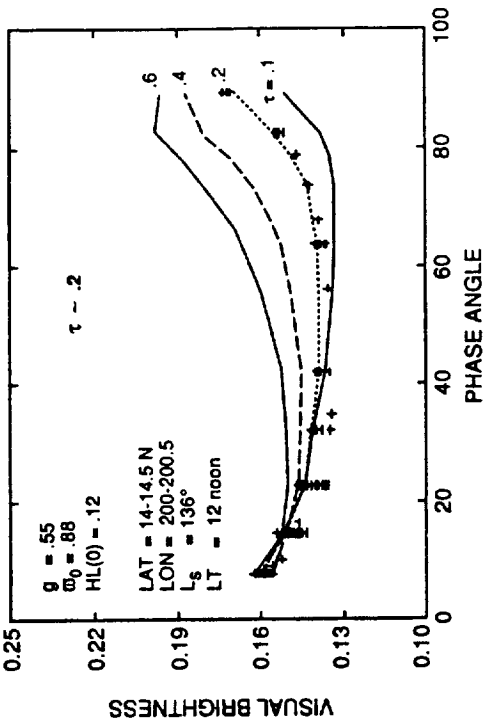

Fig. 2. Observed (crosses) phase function of EPF sequence over Cerberus versus model phase functions with τ=.1,.2,.4, and .6. Best-fit to data gives τ=.2, ϖ_0=.88, g=.55.

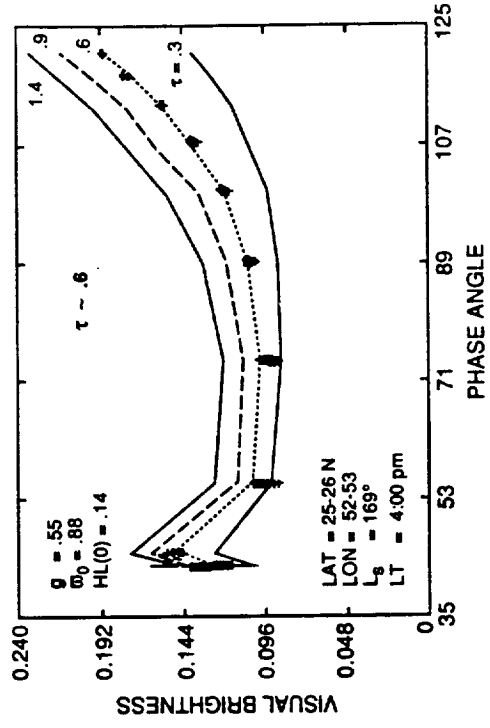

Fig. 4. Observed (crosses) phase function of EPF sequence over Chryse Planitia versus model phase functions with τ=.3,.6,.9, and 1.4. Best-fit gives τ=.6, ϖ_0=.88, g=.55.

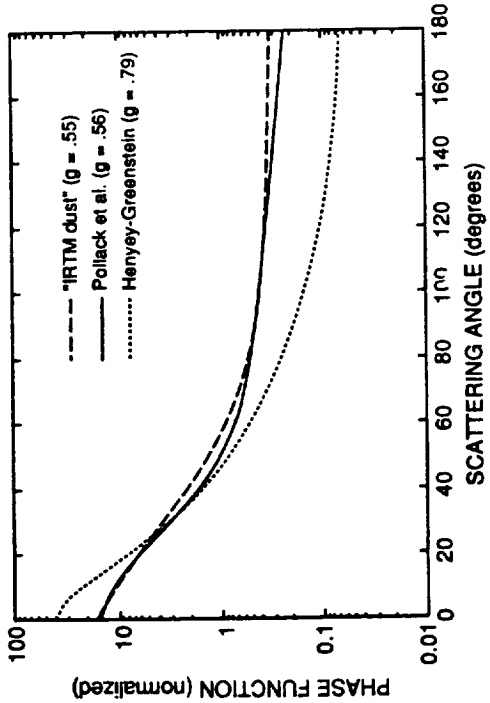

Fig. 1. Mars aerosol phase functions.

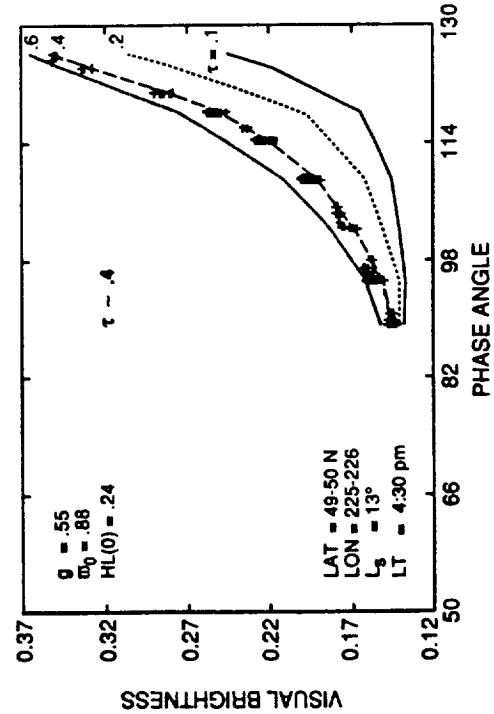

Fig. 3. Observed (crosses) phase function of EPF sequence over Utopia Planitia versus model phase functions with τ=.1,.2,.4, and .6. Best-fit to data gives τ=.4, ϖ_0=.88, g=.55.

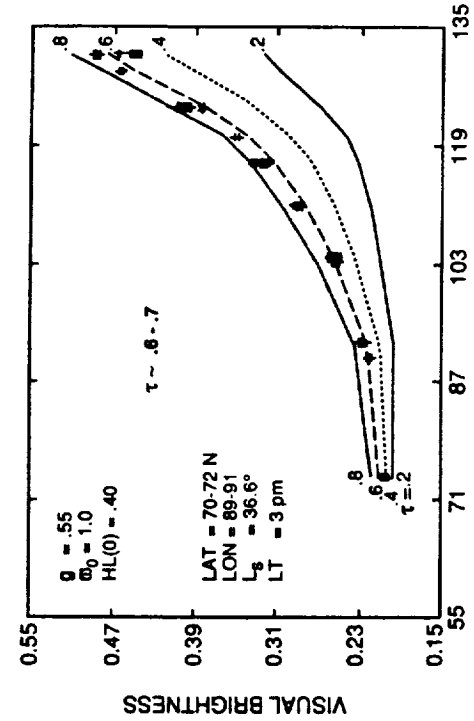

Fig. 5b. Observed (crosses) phase function of EPF sequence over the North polar erg versus model phase functions with τ=.2, .4,.6, and .8. Best-fit to data gives τ=.7, ϖ_0=1.0, g=.55.

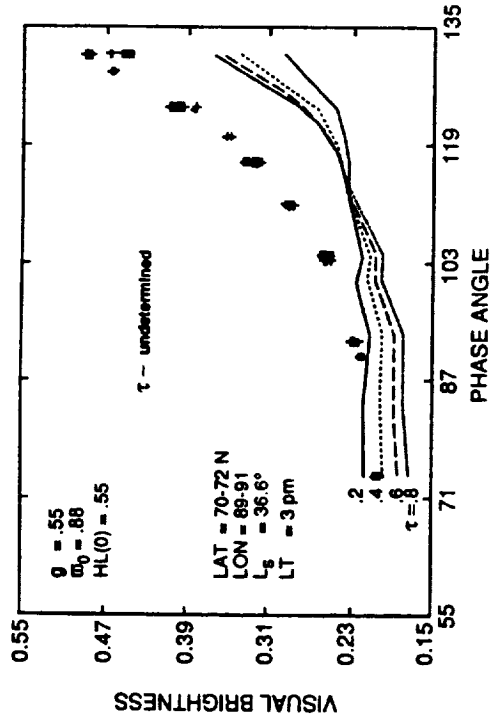

Fig. 5a. Observed (crosses) phase function of EPF sequence over the North polar erg versus model phase functions with τ=.2, .4,.6, and .8. No fit is possible for ϖ_0=.88, g=.55.

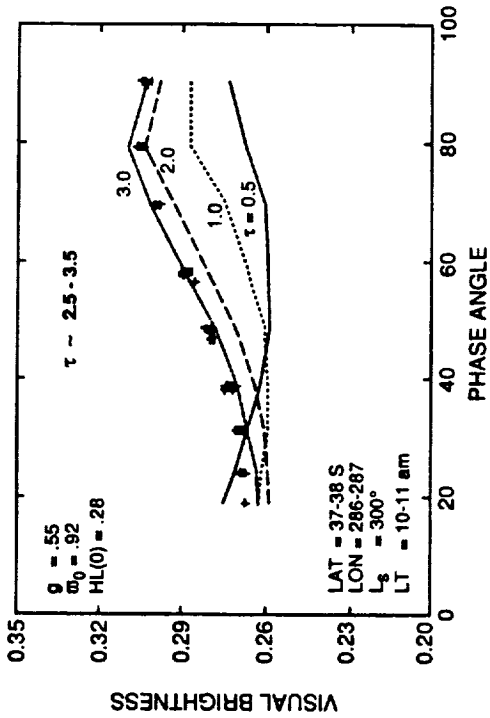

Fig. 6b. Observed (crosses) phase function of EPF sequence over Hellas Planitia versus model phase functions with τ=.5,1.0, 2.0, and 3.0. Best-fit gives τ=3.0, ϖ_0=.92, g=.55.

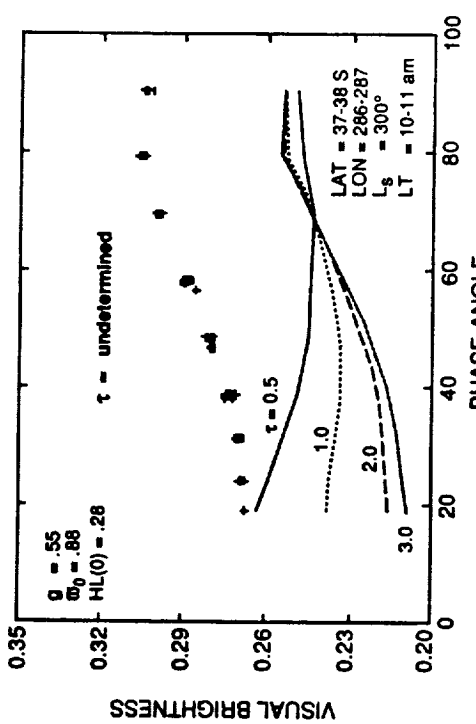

Fig. 6a. Observed (crosses) phase function of EPF sequence over Hellas Planitia versus model phase functions with τ=.5,1.0, 2.0, and 3.0. No fit is possible for ϖ_0=.88, g=.55.

COLD POLAR DESERTS: WEATHERING RATES, MECHANISMS, AND IMPLICATIONS FOR REMOTE SENSING OF MARS; Edward A. Cloutis, Department of Geology, University of Alberta, Edmonton, Alberta T6E 4S6

Introduction: Polar and alpine desert regions (cold deserts) offer the best terrestrial field analogues to weathering conditions on Mars [1]. A suite of rock samples from the Northwest Territories in Canada has been spectrally characterized in order to better understand the weathering processes prevalent in cold deserts and to examine the implications for remote sensing of Mars. Since these samples have presumably been subaerially exposed only since the last period of glaciation, they are useful for examining how relatively short-term physical and chemical weathering affect spectral properties.

The samples were collected from the Yellowknife Bay area (basalt) and Contwoyto Lake-Point Lake region in the Slave Province. The samples include a basalt (JMP2), an iron formation (5PLJ009), a volcanoclastic (4PLI017), a schist (5PLT001), and a granite (5PLJ001). Both weathered (exterior) and unweathered (interior) surface spectra of each sample were measured. It is known that physical and chemical weathering operate at low rates in cold, dry deserts. The unique environment of these regions affects the relative importance of different weathering processes [2]. The most common alteration phenomona which have been amply documented are the formation of ferric iron oxides/hydroxides, as evidenced by rust-colored staining on rock surfaces and in soils [3,4,5,6], and the formation of clays [3,7,8].

Results: *Basalt:* The weathered and unweathered surface spectra of a basalt are shown in Figure 1. The weathered surface spectrum shows strong evidence of ferric iron at shorter wavelengths- an absorption edge near 0.53μm, and two broad absorption bands near 0.65 and 0.9μm. The wavelength position of the latter band (~0.88μm) and its broadness are consistent with multiple hydrated ferric species such as goethite, ferroxyhyte and ferrihydrite [9,10]. The interior surface spectrum suggests a greater ferrous iron component and is similar to other unweathered basalt spectra [11,12]. At longer wavelengths both spectra are similar. The various absorption bands can be assigned to clay lattice-OH absorption bands involving both Mg and Al, as expected for a basalt. The presence of these bands in the interior surface spectrum indicates that the interior has been slightly metamorphosed.

Iron Formation: Sample 5PLJ009 is composed of magnetite, chert and siderite. The degree of visible weathering is small enough so that the underlying banding is still visible. The weathered surface spectrum is again dominated by ferric iron absorption features. The broad band near 1.9μm indicates that weathering has produced multiple hydrated species and/or poorly-crystallized phases (Figure 2). The interior surface spectrum is dominated by siderite, which exhibits a broad absorption band between ~1.0 and ~1.4μm. However, the expected strong carbonate absorption bands at 2.35 and 2.56μm [13] are absent.

Volcanoclastic: The weathered surface spectrum of a felsic-pyritic metatuff is again dominated by ferric iron bands at shorter wavelengths (Figure 3). A broad pyrite absorption band expected near 1μm is not evident. The weakness of various clay lattice-OH bands suggest that the formation of well-crystalized hydrated species has not been significant. The interior spectrum shows almost no evidence for ferric iron absorption bands. The broad feature centered near 1.05μm is characteristic of ferrous iron and pyrite.

Schist: The weathered and unweathered surface spectra of a cordierite-biotite knotted schist differ markedly from each other (Figure 4). In both cases there is a general lack of diagnostic absorption bands. The general reflectance rise towards longer wavelengths and lack of well-defined absorption bands in the exterior spectrum suggests that weathering has generated a number of poorly crystallized phases which absorb incident radiation over a range of energies, probably through charge transfers.

Granite: Granite differs from the other samples in its general lack of iron-bearing minerals. This is reflected in the lack of ferric iron absorption bands in the spectrum (Figure 5). Both the interior and exterior surface spectra show the same types of long wavelength absorption bands, indicative of aluminum.

Discussion: In spite of the presumed low rate and duration of weathering which has presumably affected these samples, exterior (weathered) and interior (unweathered) surfaces of the same sample vary from very similar (Figure 1) to radically different (Figures 4 & 5). It is apparent that significant spectral changes can be effected by even the low weathering rates prevalent in cold desert regions. The formation of ferric iron species results in the appearance of an absorption edge near 0.53μm, a shoulder or band near 0.64μm, and an absorption band near 0.9μm [9,10]. These features are most apparent in the most iron-rich samples such as basalt, iron formation and volcanoclastic. The reflectance spectra amply confirm the physico-chemical and spectral importance of ferric iron oxide/hydroxide formation in cold deserts.

Aluminum- and magnesium-rich lithologies give rise to Al-OH and Mg-OH absorption bands respectively in weathered surface spectra in cases where the absorption bands are resolvable. For example, the absorption bands present in the exterior granite spectrum at 2.20, 2.32 and 2.35μm can be assigned to Al-OH vibrations. There is no clear evidence for an Mg-OH absorption band expected near 2.4μm. This is consistent with the aluminum-rich composition of the granite.

A general lack of well-defined absorption bands attributable to specific hydrated phases indicates that cold desert weathering is generally not accompanied by the formation of well-crystallized phases, but that clay formation is nevertheless an important process. The broadness of the ferric iron absorption bands also suggests that poorly-crystallized phases are important. The formation of poorly-crystallized phases in cold deserts is consistent with interpretations of martian telescopic spectra as indicating semi-amorphous or amorphous phases such as palagonite [14].

The spectral changes associated with cold desert weathering include variations in overall spectral slope, the appearance/disappearance of absorption bands, shifts in absorption band minima wavelength positions, and changes in band shapes and intensities. Dramatic spectral differences between interior and exterior surface spectra are present even when weathered surfaces are thin enough so that underlying petrofabrics are still visible.

In spite of the small number of samples in the current suite, the data indicate that cold desert weathering of carbonates may be sufficient to render them virtually indistinguishable. In addition, the oxidation of ferrous to ferric iron proceeds regardless of whether the iron is derived from silicates (basalt), oxides (iron formation), carbonates (iron formation), or sulfides (volcanoclastic). It is clear that unweathered, interior rock sample spectra are generally not useful for the interpretation of remote sensing data for targets such as Mars which are subject to subaerial weathering.

Acknowledgments: This study was supported by a Grant-in-Aid of Northern Research from the Boreal Institute for Northern Studies of the University of Alberta (#55-30274) and a Research Grant from the Geological Society of America (#3741-87).

References:[1] Agresti, D.G., Morris, R.V., Newcomb, J.A., and Lauer, H.V. Jr., *Lunar Plan. Sci. Conf. XVII*, 3-4 (1986). [2] Ugolini, F.C., *Rates of Chemical Weathering of Rocks and Minerals*, 193-235 (Colman & Dethier, Eds.), Academic (1986). [3] Glazovskaya, M.A., *Sci. Pap. Inst. Geol. Geogr. Sci. Moscow Univ., 1*, 63-76 (1958). [4] Tedrow, J.C.F., *Soil Sci. Soc. Amer. Proc., 30*, 381-387 (1966). [5] Ugolini, F.C., *NAS-NRC Publ. 1278*, 55-61 (1966). [6] Bockheim, J.G., *Soil Sci., 128*, 142-152 (1979). [7] Claridge, G.C.C., *New Zealand J. Geol. Geophys., 8*, 186-220 (1965). [8] Jackson, M.L., Lee, S.Y., Ugolini, F.C., and Helmke, P.A., *Soil Sci., 123*, 241-248 (1977). [9] Sherman, D.M., Burns, R.G., and Burns, V.M., *J. Geophys. Res., 87*, 10169-10180 (1982). [10] Morris, R.V., Lauer, H.V. Jr., Lawson, C.A., Gibson, E.K. Jr., Nace, G.A., and Stewart, C., *J. Geophys. Res., 90*, 3126-3144 (1985). [11] Hunt, G.R., Salisbury, J.W., and Lenhoff, C.J., *Mod. Geol., 5*, 15-22 (1974). [12] Singer, R.B., and Blake, P.L., *Lunar Plan. Sci. Conf. XIV*, 706-707 (1983). [13] Hunt, G.R., and Salisbury, J.W., *Mod. Geol., 2*, 22-30 (1971). [14] Singer, R.B., *J. Geophys. Res., 87*, 10159-10168 (1982).

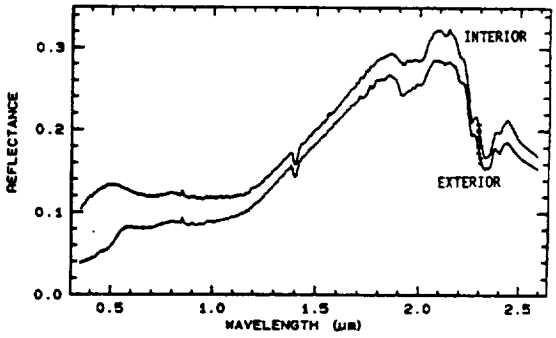

Figure 1. Reflectance spectra of interior and exterior surfaces of basalt sample JMP2.

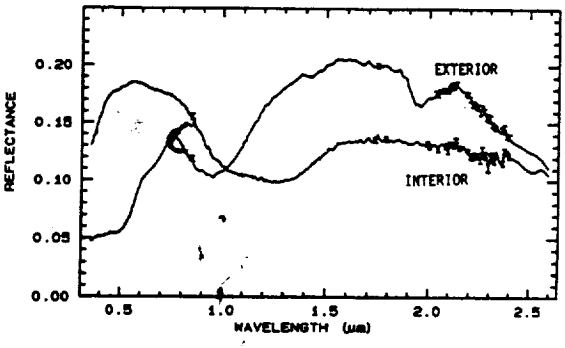

Figure 2. Reflectance spectra of interior and exterior surfaces of iron formation sample 5PLJ009.

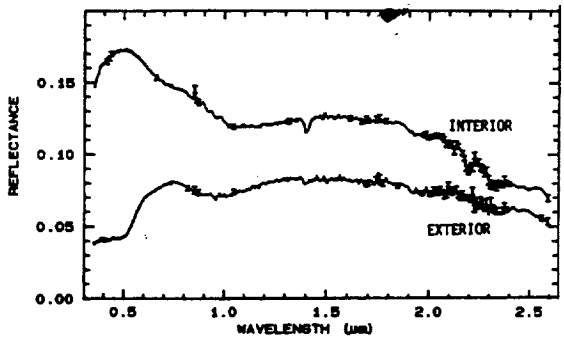

Figure 3. Reflectance spectra of interior and exterior surfaces of felsic-pyritic-metatuff (volcanoclastic) sample 4PLJ017.

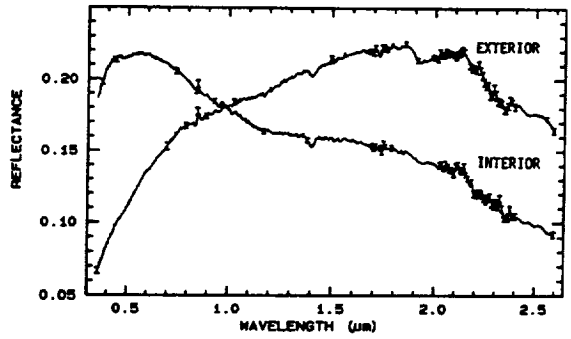

Figure 4. Reflectance spectra of interior and exterior surfaces of cordierite-biotite knotted schist sample 5PLT001.

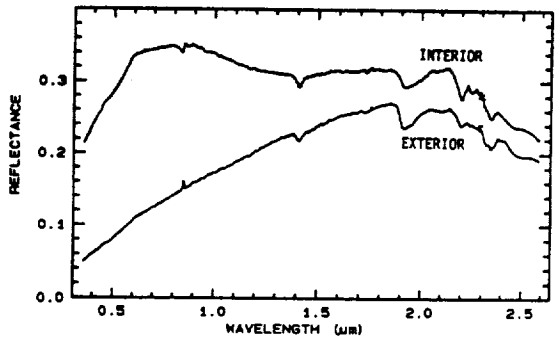

Figure 5. Reflectance spectra of interior and exterior surfaces of granite sample 5PLJ001.